

**Industry
Canada
CRC**

**A SIMULATION STUDY OF HF DIRECTION
FINDING IN THE PRESENCE OF F-REGION
SCATTERING AND SPORADIC-E**

by

R.W. Jenkins



19950131 042

CRC TECHNICAL NOTE 93-004

January 1994
Ottawa



Industry and Science Industrie and Science
Canada Canada

The work described in this document was sponsored by the Department of
National Defence under Task 1410-041XP and 1410-041BB.

DISTRIBUTION STATEMENT A

Approved for public release;
Distribution Unlimited

Canada

A SIMULATION STUDY OF HF DIRECTION FINDING IN THE PRESENCE OF F-REGION SCATTERING AND SPORADIC-E

by

R.W. Jenkins

(Radio Communications Technology Directorate)

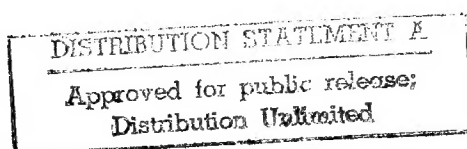
Accession For	
NTIS CRA&I	<input checked="" type="checkbox"/>
DTIC TAB	<input type="checkbox"/>
Unannounced	<input type="checkbox"/>
Justification	
By	
Distribution /	
Availability Codes	
Dist	Avail and/or Special
A-1	

The work described in this document was sponsored by the Department of
National Defence under Task 1410-041XP and 1410-041BB.

COMMUNICATION RESEARCH CENTRE INDUSTRY AND SCIENCE
CRC REPORT NO. 93-004

Canada

January 1994
Ottawa



ABSTRACT

An HF direction-finding (DF) system employing sampled-aperture techniques on high-latitude signals is simulated. The propagation is treated as scatter from moving patches of field-aligned F-region irregularities modelled as vertical "thin-wire" scatterers in a horizontally stratified ionosphere, plus a weak sporadic-E (E_s) reflection from a horizontal mirror-like surface. The resultant simulated received signals are analysed by plane wave fitting and multiple-signal classification (MUSIC) DF algorithms.

Simulations of DF operations on scattered signals, using system parameters similar to those used for actual high-latitude observations, reveal results similar to those observed. The observed directions are an indication of the locations of the scattering patches rather than the transmitter. The detection of a patch depends strongly on its location, the radio frequency, and the ionospheric parameters. When a patch is seen, the time history of estimated directions indicates its width, as well as its location. MUSIC provides a picture of the width and number of scattering patches present in a short time. Plane-wave fitting tends to give only the directions for the patch having the strongest scattered signal and requires a longer time for the successive direction estimates (spread over the angle subtended by the patch) to indicate the patch width. When too many signal directions are assumed, MUSIC gives false directions which correspond to the steered directions of the array for which the larger sidelobes are pointed toward the strongest signals. When a weaker E_s signal is present with the scattered signal, MUSIC can see it clearly and provide a good direction estimate, provided array dimensions are not so large that narrow beamwidths coupled with large-sidelobe effects prevent the weaker E_s signal from being seen.

RÉSUMÉ

Un dispositif radiogoniométrique haute-fréquence à échantillonnage d'ouverture est simulé pour le cas des signaux que l'on retrouve aux haute latitudes. Dans la simulation on considère que la propagation des signaux est le résultat de la dispersion des signaux par des zones non-uniformes et mouvantes de multiples conducteurs minces dans la couche F alignés sur le champ magnétique terrestre. Ces zones sont représentés dans la simulation par des fils conducteurs minces agissant comme éléments dispersifs dans une ionosphère stratifiée horizontalement, auxquels on ajoute l'effet d'une réflexion faible provenant de la couche sporadique E (E_s) représentée dans la simulation par un miroir horizontal. Les signaux résultants sont analysés par le moyen d'algorithmes impliquant ajustement d'ondes planes et classification de signaux multiples (appelés MUSIC pour Multiple Signal Classification).

Les résultats obtenus à la suite de simulations de systèmes radiogoniométriques opérant sur signaux de dispersion permettent d'obtenir des résultats conformes aux mesures aux hautes latitudes. Les résultats de la goniométrie révèlent que les directions de provenance des signaux correspondent aux zones de dispersion et non à la position de l'émetteur. La détection d'une zone de dispersion dépend principalement de sa position, de la fréquence radio utilisée et des paramètres physiques de l'ionosphère. L'historique de l'observation de la direction d'une zone de dispersion permet d'en déduire la largeur et la position. Le système MUSIC permet d'obtenir une représentation, pour une courte période de temps, de la largeur et du nombre de zones de dispersion. La technique d'ajustement d'onde plane permet seulement de déterminer les directions successives de la zone dispersive produisant la plus grande intensité de signal. En outre, cette technique exige un temps plus considérable de calcul en ce qui a trait à l'estimation (s'étalant sur l'angle sous-tendu par la zone de dispersion) des directions successives des signaux provenant des zones de dispersion pour en arriver au calcul de la largeur de la zone. Quand trop de directions de signaux incidents sont présumées le système MUSIC produit de faux résultats. Les directions ainsi obtenues correspondent à l'alignement de lobes latéraux avec les signaux les plus intenses. Le système MUSIC permet la détermination de la direction de signaux faibles E_s (parmi les signaux forts de dispersion) pourvu que les dimensions du réseau d'antennes soient telles que le faible étalement du faisceau principal combiné aux effets dus aux lobes latéraux n'en préviennent la détection.

EXECUTIVE SUMMARY

The operation of a sampled-aperture HF direction-finding system at high latitudes is considered. The irregular, drifting ionosphere present at high latitudes provides the conditions for the creation of patches of field-aligned irregularities, which scatter radio waves. This scattering can cause radio signals to be received from directions well removed from the great-circle bearing of the transmitter. A feature which may also be present some of the time that scattering occurs is sporadic-E. Sporadic-E reflections result in radio propagation close to the great-circle, allowing an accurate bearing estimate to be made.

A model is developed for the scatter-supported ionospheric radio propagation, along with the sporadic-E propagation. The major assumptions underlying the model are the concept of 'scattering centers', or single locations where all the scattering for a particular path is assumed to take place, and a horizontally stratified ionosphere. Although these assumptions are an oversimplification of the actual high-latitude situation, they do permit a first-order analytic model to be developed, from which some insight into the actual situation can be gained. The scattering centers are assumed to exist in 'patches' of limited horizontal extent, consistent with knowledge of the high-latitude ionosphere.

The direction-finding operation is also modelled. This includes a two-dimensional array of antennas, and a direction-finding algorithm which obtains direction estimates from the signal samples received at the array elements. Two algorithms are modelled: a plane-wave fitting algorithm, which obtains a single direction corresponding to the best plane-wave fit to the received signal samples, and a MUSIC algorithm, which is capable of obtaining a number of signal directions from a set of signal samples.

DF system operation is simulated by running the model a number of times, with the scattering patch locations shifted a small amount each time, to simulate ionospheric drift motions. The resultant time histories of estimated bearing and elevation are then examined to determine the appearance of the scattering and sporadic-E features, and the performance of the system.

A particular set of simulations were used to study the time history of the observed signal directions from scattering, for various scattering-patch geometries and propagation parameters such as ionospheric electron density. The transmitter and receiver conditions simulated were similar to those of the Kestrel measurements conducted at Alert for transmissions from Thule, in November 1990. The Kestrel measurements used a plane-wave fitting technique to obtain direction time histories. Likewise, the simulations used plane-wave fitting to derive direction time histories which may be compared to those of Kestrel.

It was found from these simulations that the signal from an extended patch fits a plane wave quite well most of the time, with the arrival direction coming from anywhere inside the patch. Consecutive estimates yield different directions that are distributed over the angle subtended by the patch at the receiving array, so that a rough estimate can be obtained of the size of the scattering patch. The appearance of the time histories was similar to many of the Kestrel records. The spread in bearing observed in the simulations is substantially greater than the spread in elevation, a feature noted in many of the Kestrel records as well. The ionospheric propagation

determines the portion of the ionosphere wherein a scattering-center can be located which will contribute to the propagation. For a horizontally stratified ionosphere, the contributing scattering centers are limited to a strip, perpendicular to the direct transmit-receive path and centered on its midpoint. For an irregular ionosphere, the allowed contributing region could be quite different. With moving scattering patches, the patches are seen only where they pass through the allowed region. When two or more patches are present, the patch which has the strongest composite scattered signal at the receive array will control the estimated direction. With random scattering processes, the signal received from any one patch can vary substantially from estimate to estimate, so that when two patches are fairly close in their mean signal power, the estimated direction jumps back and forth between patches, allowing both of them to be seen.

When the plane-wave fitting procedure was replaced by the MUSIC algorithm, the scattering simulations showed a generally improved result. Because a number of signal directions are obtained for a single estimate, it becomes possible to get a clear picture of the number and extent of the scattering patches with only a very short sequence of estimates. One problem that was observed with MUSIC, however, is the occasional presence of false directions that occur when too many assumed signal directions are used. These false directions correspond to array directions for which a major sidelobe of the array is directed toward the stronger signals.

The simulations which include sporadic-E as well as scattering propagation clearly show that the MUSIC algorithm can be used quite effectively to enable relatively weak sporadic-E signals to be seen in the presence of strong scattered signals. This holds some promise for high-latitude direction finding, since the sporadic-E signals are expected to be quite representative of the true bearing to the transmitter while the scattered signals are not. The masking of weaker sporadic-E signals by the array sidelobe response to stronger scattered signals is a possibility, especially when the array beamwidths are much narrower than the range of directions the scattered signals arrive from. It is therefore important to avoid large-aperture sparsely-filled arrays which have strong sidelobes. Three array geometries were tested: a the Kestrel array consisting of 7 elements with a constant radius of 25 m, the 10-element middle portion of the (Vortex) log-spiral array currently installed at CRC with a spiral radius varying from 27.5 to 175.0 m, and the 8-element inner portion of the Vortex array with a spiral radius varying from 14.8 to 62.9 m. The best simulated result were attained for the inner 8 elements of the Vortex array. With this array, at an operating frequency of 8 MHz, it was possible to obtain accurate directions for sporadic-E signals 21 dB below the scattered signals. A number of the assumed signal directions are taken up by the signals scattered by the extended scattering patches, so it is important to have enough assumed signal directions. Too many directions will result in false signal direction estimates, as a result of the array sidelobe effect. Since the number and extent of the scattering patches are not known beforehand, it is important that an operational system try various numbers of assumed signal directions, in order to obtain a good result.

TABLE OF CONTENTS

	ABSTRACT	iii
	RÉSUMÉ	v
	EXECUTIVE SUMMARY	vii
	TABLE OF CONTENTS	ix
1.0	INTRODUCTION	1
2.0	THE PROPAGATION MODEL	5
2.1	Overview	5
2.2	Generating Scatterers	6
2.3	Propagation Geometry	7
2.4	Modelled Ionosphere	8
2.5	Propagation Path Calculation	9
2.6	Signal Strength Calculation	10
2.6.1	Mean Received Power for a Ray Path	10
2.6.2	Effective Scattering Width	13
2.6.3	Generating a Sequence of Signal Samples	14
2.7	Sporadic-E Propagation	15
3.0	DIRECTION-FINDING SYSTEM MODEL	16
3.1	Plane-Wave Fitting Procedure	16
3.2	MUSIC Algorithm	17
4.0	TESTS OF THE FIELD-ALIGNED SCATTERING MODEL WITH PLANE-WAVE FITTING	19
4.1	Operational Parameters	19
4.2	Simulation Results	19
4.2.1	Single Scattering Patch	19
4.2.1.1	Dependence on Ionospheric Electron Density	22
4.2.2	Effective Scattering Region	26
4.2.3	Variation of Scattering Efficiency with Height	28
4.2.4	Multiple-Patch Case	28
4.2.4.1	Initial Simulations	29
4.2.4.2	Dependence on Ionospheric Electron Density	30
4.2.5	Effect of Different Geometries	32
4.3	Summary and Discussion of Findings	34

5.0	TESTS OF THE MUSIC ALGORITHM APPLIED TO THE FIELD-ALIGNED SCATTER MODEL	36
5.1	Single Scattering Patch	36
5.1.1	Test Parameters	36
5.1.2	Simulation Results	37
5.2	Two Scattering Patches	39
5.2.1	Test Parameters	39
5.2.2	Test Results	39
5.3	Summary and Discussion of Findings	41
6.0	TESTS OF THE MUSIC ALGORITHM APPLIED TO FIELD-ALIGNED SCATTERING AND SPORADIC-E	42
6.1	Test Parameters	42
6.2	Test Results	43
6.2.1	Single Scattering Patch, Sporadic E and Kestrel Array Geometry	43
6.2.2	Two Scattering Patches, Sporadic E and Kestrel Array Geometry	45
6.2.3	Effect of Antenna Array Geometry	47
6.2.4	Dependence on Relative Signal Strength	49
6.3	Summary and Discussion of Findings	50
	ACKNOWLEDGEMENTS	xi
	REFERENCES	xi

1.0 INTRODUCTION

The simulation studies presented here are an attempt to model the operation of a sampled-aperture HF direction-finding (DF) system operating at high latitudes. The goal of this work is two-fold: to obtain propagation models that are representative of high-latitude conditions, and to test various DF methods against those models to establish their utility.

HF direction-finding systems depend on radio propagation and therefore the condition of the ionosphere through which HF signals must pass in order to be seen. At high latitudes, the ionosphere is highly changeable, so that its effect on HF radio propagation is especially pronounced.

The high-latitude ionosphere, which includes both the polar cap and auroral regions, is governed by the interaction between the solar wind and the earth's magnetosphere. The ionosphere is located above the neutral atmosphere. The earth's magnetic field lines pass through the ionosphere, and extend upward into the magnetosphere. Any interaction-generated motions which occur in those field lines are mapped down onto the ionosphere. These motions are thought to take the form of a two-cell convective pattern, whose direction is mainly antisunward across the polar cap region covering the poles, and sunward at the auroral and subauroral regions equatorward of the polar cap [1, 2]. The ionosphere in the polar cap tends to be more irregular during darkness, since the most steady source (photoelectron production) and the main irregularity decay mechanism (E-layer conductivity) have ceased at those times. A prominent feature of the nightside polar cap ionosphere is the large-scale blobs of enhanced electron density convecting antisunward from the dayside [3]. At the same time, the moving gradients associated with these blobs give rise to short-lived small-scale irregularities whose locations move with the same convective flow [3].

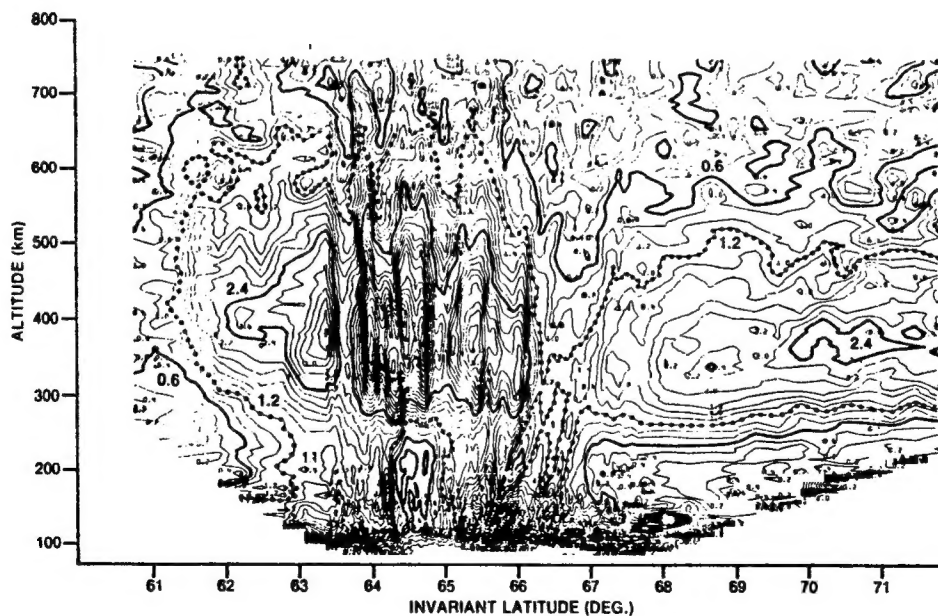


Figure 1. Electron-density contour plot of the high-latitude ionosphere, obtained by the Chatanika incoherent radar, for Feb. 20, 1981, during local night (1130-1144 UT) [4].

Figure 1 is a contour plot of the high-latitude ionospheric electron density, taken by the Chatanika, Alaska incoherent radar facility [4]. The figure is a vertical north-to-south cut through the night portion of the ionosphere, showing the subauroral region (61 to 63.5° N), the auroral region (63.5 to 66.5° N), and a portion of the polar cap (above 66.5° N). The strongest horizontal gradients are seen in the auroral region. Significant large-scale irregular features are also seen in the polar cap region which is of major interest to the present work.

The implications for HF radio propagation are substantial. Radio waves will be reflected obliquely from large and medium-scale irregularities of several km extent or greater (one Fresnel zone for HF radio waves). They also will be scattered from smaller-scale irregularities which have sizes less than one km. The larger-scale features are expected to be sufficiently long-lived that in their lifetimes they will move substantially with the general high-latitude convective flow[5]. The smaller irregularities last several seconds or less[6]. These irregularities exist in patches in the vicinity of the large-scale gradients which drift with the convective flow.

Two complementary models for high-latitude radio propagation have been developed in the current study program. The first model is based upon reflection of radio waves from large and medium scale irregularities and treats the irregular ionosphere as a bumpy-mirror reflecting surface. The bumps were modelled as fixed and occurring in patches which moved with a constant horizontal motion typical of high-latitude drift motions. The second model is based upon aspect-sensitive scattering from the small-scale irregularities. These models have been presented in technical memoranda [7, 8].

A currently available source of high-latitude DF data is that of the Kestrel program [9, 10]. This program consisted of a two-week measurement campaign utilizing seven elements of the Alert pusher array together with an Andrew Corp. sampled-aperture receiving and processing system. This system performed a real-time phase-front analysis on the sampled signals from the array, to obtain the best-fit plane-wave bearing and elevation which were recorded along with a measurement quality index denoted as the WSPI, several times a second. These recordings form a permanent record against which the predictions of models can be tested. The most helpful measurements for establishing high-latitude propagation conditions are those taken on the 8.05 MHz transmissions from Thule, 667 km distant. They provide a propagation path lying well within the polar cap at all times of day.

Both the bumpy-mirror and aspect-sensitive scattering models were tested against a plane-wave fitting DF procedure, using an array and transmitter geometry similar to that of the Kestrel data for Thule [7, 8]. This provided a means of comparing the predictions of these models against observed data. Both models predict a spread in the consecutive arrival directions found with a plane wave estimator, and a change in direction corresponding to the general motion of a bumpy region or region of scatterers. These predictions are consistent with the Kestrel observations. However, the bumpy-mirror model by its nature imposes a large spread in elevation when the spread in azimuth is large [7], while the scattering model imposes a much smaller elevation spread because of the selective nature of aspect sensitivity [8]. In this regard, the Kestrel data is more supportive of the scattering model [9]. Also, the scattering model predicts that different scattering regions will be visible in a sequence of consecutive direction estimates [8], which appears to be the case at least part of the time. The bumpy-mirror model predicts a more abrupt

transition in the visibility of two moving disconnected bumpy regions as their relative strengths change [7]. Nonetheless the bumpy-mirror model does predict one unique feature which is seen in the data at times: the occasional clustering of directions (associated with randomly-occurring strong focusing from a single reflecting location). The bumpy-mirror model is not considered further in this report.

One propagation mode not included in the models [7, 8] but seen in the Kestrel data is that of sporadic-E (E_s) [9]. This mode occurred only rarely in this data, and lasted only for several minutes at a time. However, the direction estimates obtained with this mode were much more accurate than the estimates obtained at other times. The DF plane-wave fitting technique employed in this data permitted the E_s mode to be seen only if its signal strength was comparable to or exceeded that of other modes. In view of the improved accuracy for this mode, other sampled-aperture DF techniques should be considered if they allow the E_s mode to be seen when it is lower in strength than the remaining modes. A class of algorithms typified by MUSIC [11] fall into this class. These algorithms permit a number of arrival directions to be ascertained from a single set of data, even when the corresponding signal levels are quite different in their strengths.

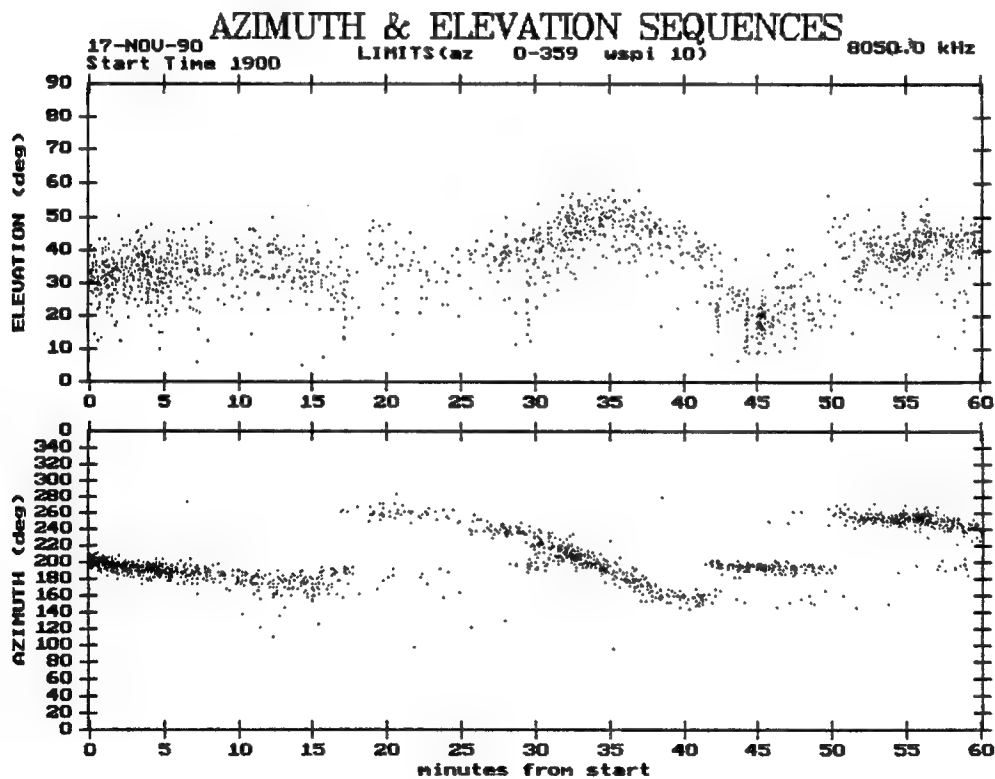


Figure 2. Kestrel azimuth and elevation time histories for the Thule 8.05 MHz transmissions.

An example of the Kestrel data is given in Figure 2, which shows the tracking of a moving scattering region, the spread of its estimated arrival directions, and the brief appearance of the E_s mode from 42 to 50 minutes from the start. The E_s mode is characterized by its closeness in

azimuth to the great-circle direction (194° E of N) and its lower elevation angles (as compared to the F-layer returns seen at other times).

The present formal report includes a description of the scattering model used. The model is extended beyond the single-sample model presented previously [8] so that it may be used with DF algorithms such as MUSIC which require more than one sample of the signals across the antenna array.

The predictions of the extended scattering model for sampled-aperture DF arrays are presented, using both a plane-wave fitting DF procedure and the MUSIC algorithm. These predictions are of prime interest, in determining the validity of the scattering model in comparisons with acquired data and in assessing its effect on the performance of the two DF algorithms.

In a second series of simulations also included in this report, a sporadic-E propagation mode has been added to the scattering. The prime concern here is with the performance of a DF system in the presence of an 'extended-source' or 'many-path' propagation mode such as scattering, along with the fixed single-path E_s mode. The MUSIC algorithm is tested for its ability to see the E_s mode when its signal is much weaker than that of the scattered signal. Various algorithm and antenna configurations are tested to determine which are most effective under these conditions.

2.0 THE PROPAGATION MODEL

2.1 Overview

The propagation model is comprised of two parts: F-layer scattering and sporadic-E propagation. A flat earth is assumed. The F-region is assumed to be horizontally stratified and parabolic in its height profile. The effect of collisions and the magnetic field on radio wave propagation are neglected, resulting in a real isotropic refractive index [12]. The E-region is assumed to be a flat horizontal reflector, with a specified power reflection coefficient. A transmitting and a receiving location are specified, along with a receiving array geometry and the elevation patterns of the transmitting and receiving antennas.

The direction-finding system modelled is a sampled-aperture array, with either a plane-wave fitting algorithm or the MUSIC [11] algorithm applied to the signal samples. The plane-wave fitting algorithm requires only a single sample from each antenna, and provides a single direction estimate. The MUSIC algorithm requires a number of consecutive samples be taken from each antenna, and permits more than one signal direction to be estimated from these samples.

The modelled scattering occurs in the F-layer, in specified regions or patches which contain a specified density of vertically-aligned 'scattering centers'. These scattering centers are introduced in order to replace the multiple-scattering problem by the more tractable single-scattering problem. This approach is partially justified by noting that for vertically-aligned elongated scatterers of small horizontal dimension, a singly-scattered wave has the same elevation angle as the original wave and a completely arbitrary azimuth, i.e., the incident wave is scattered equally into all azimuths. As a result, multiple scattering also preserves the elevation angle and the energy is scattered equally into all azimuths, regardless of the number of scatters. The scattering centers replace the scattering that occurs at several places along the path of a particular ray by a single scattering occurring at the location of the scattering center. The propagation process is described further in Section 2.3. The energy intercepted by a scattering center is scattered equally into all azimuths, while the elevation angle is preserved. A height-dependent 'scattering width' representing the scattering efficiency is introduced for each scattering center. Given a particular scattering center, under the assumption of a horizontally stratified ionosphere the potential propagation paths have a common projection on the horizontal plane, consisting of a straight line from the transmitter to the base of the scattering center and another from the scattering center to the receiver.

Each scattering center generated by the model is considered separately in terms of its contribution to the total signal seen at the receiving array. The MUSIC algorithm requires a series of consecutive signal samples in order to obtain a non-singular covariance matrix from which the directions are estimated. In practice these samples would be close in time, perhaps a fraction of a millisecond apart. The scatterers themselves may have time constants of the order of a tenth of a second or more. In order to simulate the time changes and generate consecutive samples, the contribution of each scattering center is modulated in its phase and amplitude by narrowband white noise, the bandwidth of which is set according to the Doppler spreading anticipated on high-latitude HF circuits. The actual locations of scattering centers are considered constant over a series of consecutive signal samples.

The simulation is performed for a number of estimates, to simulate direction-finding on a particular signal over a period of time. These estimates are taken from separate sets of samples, between which the patch locations have shifted by a specified constant amount in order to simulate high-latitude ionospheric convection. For each set of samples, the actual locations of the scattering centers within each patch are generated anew. The parameters, such as scattering-center density and patch dimensions, are assumed to remain constant over a simulation run.

2.2 Generating Scatterers

In the flat-earth geometry of the model, a scattering center location is expressed by its horizontal coordinates x, y . Each center is vertically oriented, and can be considered to exist at all heights h . The scattering regions or patches are assumed rectangular so that they can be specified by their x and y coordinate ranges x_0 to x_1 , y_0 to y_1 .

For a given mean density of scattering centers ν , the probability of a scatterer existing in an infinitesimally narrow strip dx wide between y_0 and y_1 is given by

$$p(x) dx = \nu (y_0 - y_1) dx \quad (1)$$

This results in the scattering centers being distributed in their x -coordinate according to a Poisson distribution, so that the distance d_x along the x -axis from x_0 to the first scattering center, and between succeeding centers, is governed by the distribution function

$$P(d \geq d_x) = \exp(-\nu (y_0 - y_1) d_x) \quad (2)$$

The Monte Carlo method is used to compute the distance along the x -axis to the first scattering center and between succeeding centers. Equation (2) is inverted, and $P(d \geq d_x)$ is replaced by independent computer-generated random numbers $N_{rand}(i)$ uniformly distributed between 0 and 1. The x -axis separations are then given by

$$d_x(i) = \frac{\log(N_{rand}(i))}{\nu (y_0 - y_1)} \quad (3)$$

where the index i indicates the i th scattering center. Thus the x -coordinate of the i th center is given by

$$\begin{aligned} x_s(i) &= x_0 + d_x(1) & \text{for } i = 1 \\ x_s(i-1) + d_x(i) & & \text{for } i > 1 \end{aligned} \quad (4)$$

The x -coordinates are generated sequentially according to equation (4), until x_1 is exceeded. The corresponding y -coordinates are distributed uniformly between y_0 and y_1 so that

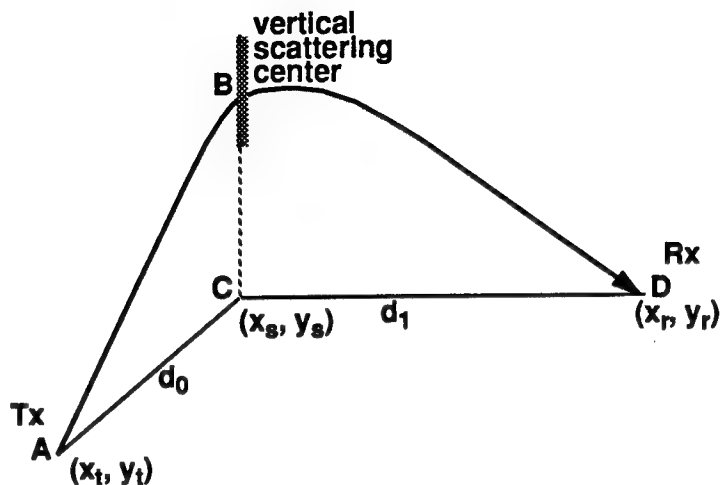
$$y_s(i) = y_0 + (y_1 - y_0) N'_{rand}(i) \quad (5)$$

where the $N'_{rand}(i)$ are likewise independent computer-generated random numbers between 0 and 1.

2.3 Propagation Geometry

The propagation geometry of the model is illustrated in Figure 3. For a particular successful

Figure 3. Propagation geometry showing transmitter, scattering center, and receiver locations.



path, the ray leaves the transmitter at point A of this figure, and is refracted as it passes through the ionosphere, where it meets a scattering center of vertically-aligned scatterers at point B. The scattered rays are constrained to have the same zenith angle as the incident ray, but are free to have any azimuth angle. The ray reaching the receiver is thus scattered into the appropriate azimuth in which it continues to be refracted, eventually turning downward so it eventually leaves the ionosphere and arrives at the receiver (point D). The two planes of propagation defined by the transmitted ray and the vertical scattering center, and the received ray and scattering center meet at the line BC defined by the scattering center. The problem can be simplified by considering the two propagation planes as a single plane, folded about the line BC. This single plane is then flattened so that the whole path can be plotted in two dimensions, as shown in Figure 4.

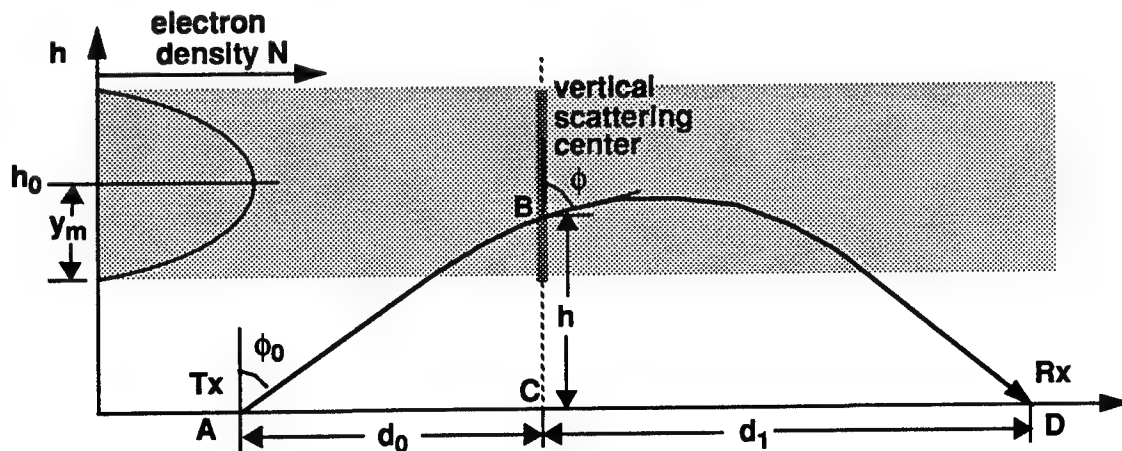


Figure 4. Propagation geometry in the unfolded plane of propagation, showing the parabolic electron density profile.

Figure 4 shows the unfolded propagation path described above, along with the vertical scattering center. The preservation of elevation angle (or its complement the zenith angle ϕ) in the scattering process is clear, so that the equation of the scattered path is the same as that of a ray transmitted at the same elevation angle and refracted (but not scattered) by the ionosphere so it arrives at the ground at a point separated from the transmitter by a horizontal distance which is the sum of the distances from transmitter to scattering center and scattering center to receiver.

The transmitter location is defined by its (x,y) coordinates (x_t, y_t) . Likewise the receiver location is given as (x_r, y_r) . For a scattering center located at (x_s, y_s) , the distances d_0, d_1 of Figure 4 are found from

$$\begin{aligned} d_0 &= ((x_s - x_t)^2 + (y_s - y_t)^2)^{1/2} \\ d_1 &= ((x_s - x_r)^2 + (y_s - y_r)^2)^{1/2} \end{aligned} \quad (6)$$

and the horizontal distance from transmitter to receiver is

$$D = d_0 + d_1 \quad (7)$$

2.4 Modelled Ionosphere

The ionosphere is modelled as a single F-layer with a parabolic electron density profile is given by

$$N(h) = \begin{cases} N_0 \left(1 - \left(\frac{h - h_0}{y_m} \right)^2 \right) & \text{for } h = h_0 - y_m \text{ to } h_0 + y_m, \\ 0 & \text{elsewhere,} \end{cases} \quad (8)$$

where N_0 is the maximum electron density, h_0 the corresponding height of maximum, and y_m the ionospheric halfwidth, shown in Figure 4. The refractive index μ , ignoring collisions and magnetic field effects [12], is given by

$$\mu^2 = 1 - \left(\frac{f_p}{f} \right)^2 \quad (9)$$

where f_p is the plasma frequency given by

$$f_p^2 = \frac{Ne^2}{4\pi^2\epsilon_0 m} \quad (10)$$

where e, m are the electron charge and mass, and ϵ_0 is the permittivity of free space. From equations (8), (9), and (10), the refractive index μ can be expressed in terms of the ionospheric parameters by

$$\mu^2 = 1 - \rho^2 + \chi^2, \quad \text{where } \rho = \frac{f_0}{f} \text{ and } \chi = \rho \left(\frac{h - h_0}{y_m} \right) \quad (11)$$

for heights between $h_0 - y_m$ and $h_0 + y_m$. μ is equal to 1.0 elsewhere (free space). The critical frequency f_0 (which is the plasma frequency at the height of maximum) is an operator-entered

parameter, along with the height of maximum h_0 and ionospheric half-width y_m .

2.5 Propagation Path Calculation

The next step is to calculate the starting zenith angle ϕ_0 (see Figure 4) needed for a ray to propagate to a receiving array at ground distance D , and the corresponding distance focusing $\partial D / \partial \phi_0$ for that distance. The laws of refraction and the refractive index profile given by (11) are used for that purpose.

For a horizontally-stratified ionosphere, Snell's law states that for any height, $\mu \sin \phi$ is constant, where ϕ is the zenith angle, so that

$$\mu \sin \phi = \sin \phi_0 . \quad (12)$$

The horizontal distance along the ray path is denoted by d . Along the ray path, a small change in horizontal distance δd is related to a change δh in vertical distance by

$$\delta d = (\tan \phi) \delta h . \quad (13)$$

Substituting (12) in (13), we get

$$\delta d = \frac{\sin \phi_0}{\sqrt{\mu^2 - (\sin \phi_0)^2}} \delta h . \quad (14)$$

Equation (11) may be substituted in (14) and the result integrated from the transmitter to a horizontal distance d less than or equal to the midpoint distance $D/2$, to obtain

$$d = (h_0 - y_m) \tan \phi_0 + \frac{y_m}{\rho} \sin \phi_0 \log \left(\frac{\chi + (\cos \phi_0)^2 - \rho^2 + \chi^2}{\cos \phi_0 + \rho} \right) . \quad (15)$$

At the midpoint (Figure 4), the ray is horizontal so that equation (12) becomes

$$\mu_m = \sin \phi_0 , \quad (16)$$

where μ_m is the refractive index at this point. Setting $d = D/2$, and substituting equations (11) and (16) into (15), the ground distance D is found as a function of the starting zenith angle ϕ_0 :

$$D = 2(h_0 - y_m) \frac{\sqrt{1 - a^2}}{a} + \frac{y_m}{\rho} \sqrt{1 - a^2} \log \left(\frac{a + \rho}{a - \rho} \right) \quad \text{where } a = \cos \phi_0 . \quad (17)$$

For an arbitrary ground distance D there will be two solutions of (17) for ϕ_0 (high-angle and low-angle), provided that any exist at all.

In the implemented modelling software, a stepwise approach is taken to find the solutions for ϕ_0 , and at the same time to find the distance focusing $\partial D / \partial \phi_0$. The search is started with the ray that just reaches the base of the ionosphere at the midpoint distance $D/2$. The zenith angle of this ray ϕ_0 (*start*) is an upper bound for the possible zenith angles for a ray propagating to a

ground distance of D . It is given by

$$\phi_0(start) = \text{atan} \left(\frac{D}{2(h_0 - y_m)} \right) . \quad (18)$$

A check is made to see if the ray corresponding to this zenith angle penetrates the ionosphere. If it does then all lesser zenith angles will also penetrate the ionosphere and there will be no solutions. Penetration occurs when the ray can reach the height of maximum and not be bent horizontal, i.e., when $\phi(h_0) < \pi/2$. From (11) and (12), penetration occurs when

$$\cos \phi_0 > f_0/f . \quad (19)$$

Equation (19) is used to check for the existence of solutions.

The zenith angle is then incrementally reduced from the upper limit $\phi_0(start)$ and the 'search' ground distance D' found for each step from equation (17). Reference [13] provides a helpful description of path length on zenith angle. Initially the search distances D' are greater than the actual distance D , and decrease as the zenith angle is reduced (and the elevation is raised). When the search distance D' first becomes less than the actual ground distance D , that value and its corresponding zenith angle and the value for the previous step are interpolated, to find the zenith angle where $D' = D$. The interpolation takes the form of an iterative linear interpolation, with the change in zenith angle decreasing each iteration, until it reaches a limit set by the program (10^{-5} radians). The zenith angle thus obtained is the low-angle solution $\phi_0(low)$. The distance focusing parameter $\partial D / \partial \phi_0(low)$ is also found by this interpolation procedure.

The stepping downward in zenith angle (i.e., increasing in elevation) is then continued. The search distances D' continue to decrease for a number of steps, to a minimum value (the skip distance) after which they begin to increase. The point at which D' again becomes greater than D is noted. That point and the previous point are interpolated as before to find the high-angle zenith angle $\phi_0(high)$ and focusing parameter $\partial D / \partial \phi_0(high)$.

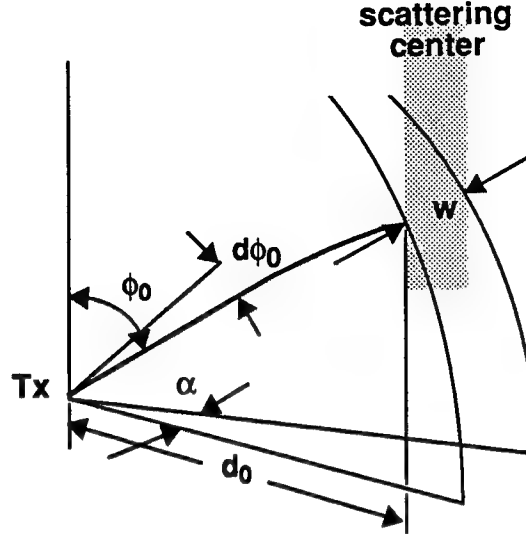
It should be noted that when the transmitted frequency is well below the maximum useable frequency (MUF) for the distance D , the zenith angle for the high-angle ray will be less than one step above 0° . The step-search procedure will fail in such cases, as a step decrease in the zenith angle will reduce it to a value less than zero, which is physically impossible. These cases can be safely ignored, as the focusing parameter $\partial D / \partial \phi_0$ becomes extremely large for the high-angle ray at frequencies well below the MUF and, as will be seen in the next section (equation (28)), this results in a very low signal strength. In such cases the high-angle ray is not included.

2.6 Signal Strength Calculation

2.6.1 Mean Received Power for a Ray Path

For each valid path, the simulation program computes the mean signal power, and a sequence of signal-sample contributions at the receiving array. This calculation depends on the geometry, ionospheric focusing, and scattering efficiency.

Figure 5. Transmitter-to-scattering center geometry showing subtended angles.



A single vertical scattering center may be considered to have a cross section per unit length or 'scattering width' w , which can be treated as a horizontal distance. As shown in Figure 5, it subtends an angle α at the transmitter, given by

$$\alpha = \frac{w}{d_0}. \quad (20)$$

The transmitted power radiated into this angle will be reradiated by the scattering center. For an incremental change in zenith angle $d\phi_0$ at the transmitter, the corresponding solid angle which includes the scattering center is

$$d\Omega = \alpha \sin \phi_0 d\phi_0 = \frac{w \sin \phi_0}{d_0} d\phi_0. \quad (21)$$

The power radiated into $d\Omega$ is

$$dP_s = \frac{P_t G_t d\Omega}{4\pi} \quad (22)$$

where P_t , G_t are the transmitter radiated power and antenna gain respectively. Combining (21) and (22), the following is obtained:

$$dP_s = \frac{P_t G_t w \sin \phi_0}{4\pi d_0} d\phi_0. \quad (23)$$

Note that the power dP_s will be reradiated by the scattering center equally into all azimuths, with no change in the zenith angle. The scattering-center-to-receiver geometry is illustrated in Figure 6. At the receiving array, the change in zenith angle $d\phi_0$ corresponds to a horizontal distance

$$dD = |\partial D / \partial \phi_0| d\phi_0. \quad (24)$$

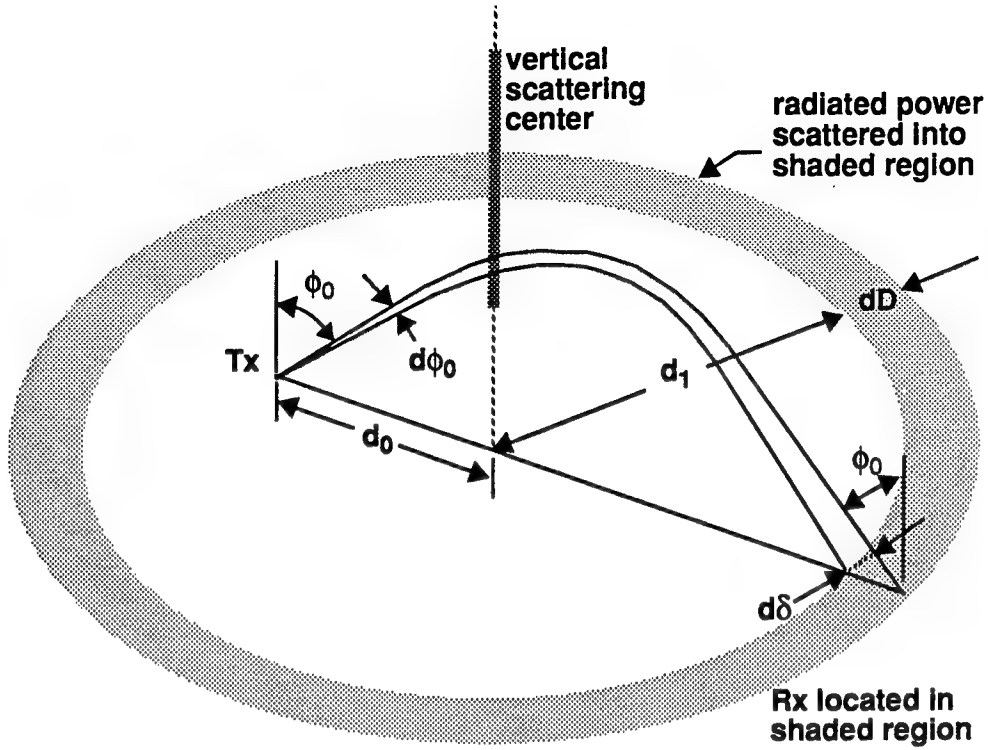


Figure 6. Scattering geometry showing region of coverage of scattered signal energy.

The corresponding distance perpendicular to the ray direction is

$$d\delta = dD \cos \phi_0, \quad (25)$$

since the symmetrical nature of the ionospheric refraction along the path implies equal transmitting and receiving zenith angles ϕ_0 . The scattered energy passes through a ring of width $d\delta$ and diameter d_1 centered on the point of intersection of the scattering center with the ground. The area of this ring, normal to the ray path, is

$$dA = 2\pi d_1 d\delta = 2\pi d_1 \cos \phi_0 \left| \partial D / \partial \phi_0 \right| d\phi_0. \quad (26)$$

From (23) and (26), the power density at the receiving array is found to be

$$S_r = \frac{dP_s}{dA} = \frac{P_t G_t w \tan \phi_0}{8\pi^2 d_0 d_1 \left| \partial D / \partial \phi_0 \right|}. \quad (27)$$

The received power, for an array element antenna of gain G_r , is then

$$P_r = \frac{S_r G_r \lambda^2}{4\pi} = \frac{P_t G_t G_r \lambda^2 w \tan \phi_0}{32\pi^3 d_0 d_1 \left| \partial D / \partial \phi_0 \right|}. \quad (28)$$

It remains to specify the effective scattering width w as a function of height and time, before the rms signal strength can be obtained.

2.6.2 Effective Scattering Width

The physical processes involved in the actual radio wave scattering determine the dependence of effective scattering width w upon the excess electron density δN and size of the scattering irregularities. A radio wave incident on a vertical field-aligned irregularity, of horizontal area A corresponding to small transverse dimensions relative to a wavelength, will by virtue of its electric field induce an excess oscillating vertical current in the irregularity proportional to the excess electrons per unit length, given by $A\delta N$. The scattered wave can be considered to be radiated by this excess current. As such, it will have an associated magnetic field \vec{B} proportional to the excess current, and therefore to $A\delta N$, and a corresponding electric field proportional to the rate of change of current which is also proportional to $A\delta N$. The power density of the scattered wave is proportional to $\vec{E} \times \vec{B}$ and therefore $(A\delta N)^2$ by the preceding arguments. In the present model, the density and sizes of the vertical scatterers in a particular region are assumed to be constant over the region, and the scattering centers, likewise constant, so that each center can be said to have an equal number of scatterers similar in their size distribution. Under these assumptions, the scattered wave from a collection of scatterers comprising a scattering center will have a mean power density proportional to the weighted mean square excess electron density of those scatterers. The effective scattering width for the scattering center must also be proportional to the mean square excess electron density.

In order to relate the scattering width w to the height of the scattering, two options have been included. In the first option, the rms excess electron density $\bar{\delta N}$ is taken to be proportional to the electron density N . (This assumption has been used by other researchers, as being the simplest assumption in the absence of experimental data [14].) Under this assumption, the scattering width w is proportional to N^2 . From (8), w can be written as a function of height, by

$$w = w_0 \left(1 - \left(\frac{h - h_0}{y_m} \right)^2 \right)^2 \quad (29)$$

where w_0 is the effective scattering width at the height of maximum electron density h_0 . In the second option, $\bar{\delta N}$ is assumed to be proportional to \sqrt{N} , so that w is proportional to N . This gives a somewhat less height-dependent scattering width, of the form

$$w = w_0 \left(1 - \left(\frac{h - h_0}{y_m} \right)^2 \right). \quad (30)$$

The proportionality constant w_0 is an operator-specified parameter.

It remains to find the height h , of the scattering, before w can be obtained. Under the scattering-center assumption, the scattering effectively takes place at a single height, corresponding to the location of the scattering center. (This is a simplification of what actually happens, since in the real world, the individual scatterers will be some distance apart, and the ray

will change heights as it passes from one scatterer to the next.) Equation (15) can be considered to give the horizontal distance d along the path, for a specified initial zenith angle ϕ_0 , as a function of the height-related variable χ , which in turn is given in terms of the height by (11). For convenience, the pertinent equations are reproduced here:

$$d = (h_0 - y_m) \frac{\sqrt{1 - a^2}}{a} + \frac{y_m}{\rho} \sqrt{1 - a^2} \log \left(\frac{\chi + a^2 - \rho^2 + \chi^2}{a + \rho} \right) ,$$

$$\chi = \rho \left(\frac{h - h_0}{y_m} \right) ,$$

where $a = \cos \phi_0$.

Rearranging (15) to obtain χ , the following expression is obtained:

$$\chi = \frac{(a - \rho)^2 e^{2\kappa} + \rho^2 - a^2}{2(a - \rho) e^{\kappa}} \quad (31)$$

where κ is given by

$$\kappa = \frac{\rho}{y_m} \left(\frac{d}{\sqrt{1 - a^2}} - \frac{(h_0 - y_m)}{a} \right) . \quad (32)$$

Rearranging (11), h is given in terms of χ , by

$$h = \frac{y_m}{\rho} \chi + h_0 . \quad (33)$$

For an identified ray path for which the initial zenith angle ϕ_0 has been obtained, equations (32), (31), and (33), in that order, are used to obtain the scattering height. Since the ray path is symmetric about point of maximum height in the unfolded plane of propagation, and the distance for which these formulas apply must be less than $D/2$, the lesser of d_0 and d_1 for the path is taken as d in (32). The effective scattering width is then calculated from (29) or (30) according to the user's requirement.

The simulation program then calculates the mean received power for the ray path from (28). Included in this calculation are the antenna gains G_t and G_r , which can be specified by the user as a function of zenith and elevation angle, in the simulation software.

2.6.3 Generating a Sequence of Signal Samples

For each scattering path, a sequence of signal-sample contributions will have the mean signal power calculated above, from which an rms amplitude can be obtained. However, the individual sample contributions will be affected in their phase and amplitude by sample-to-sample changes in the individual scatterers making up the scattering center. These changes are simulated

by employing bandwidth-limited white noise where the bandwidth is selected to be similar to the Doppler spreading observed in practice over high-latitude propagation paths (e.g., 10 or 20 Hz), according to the following procedure provided by Jorgenson[15]: The simulation program upon its initiation generates the appropriate digital filter coefficients for a fourth-order Gaussian spectral shaping filter, according to the user-specified Doppler bandwidth and sampling rate. Later, for each path, it generates a sequence of completely random complex samples of unit rms amplitude, and passes this sequence through the filter to obtain the required bandwidth-limited noise samples. These complex samples are multiplied by the rms amplitude, to generate a sequence of sample contributions for the path in question, as seen at the receiver reference point.

The sample contributions are then adjusted in their phase, according to the specified x , y position of each array element and the incoming zenith and azimuth angles, to obtain a sequence of sample contributions for each array element. The signal-sample contributions are accumulated over all paths, on a sample-by-sample basis, for each of the array elements, to generate a set of signal samples seen by the array, due to scatter propagation.

2.7 Sporadic-E Propagation

Sporadic E (E_s) propagation is simulated by assuming a horizontal mirror-like reflection at a height h_E , midway between the transmit and receive locations along the great-circle meridian. The value used for h_E is 100 km, which is typical of E_s heights. A user-specified reflection coefficient R , representing the fraction of signal power reflected, is used to specify the reflection efficiency.

The total path length L , for the modelled E_s propagation is determined by the flat-earth geometry to be

$$L = ((x_t - x_r)^2 + (y_t - y_r)^2 + 4h_E^2)^{1/2} \quad (34)$$

and the corresponding received power is

$$P_r = \frac{G_t G_r \lambda^2 P_t R}{16\pi^2 L^2} \quad (35)$$

The corresponding zenith and azimuth angles ϕ , θ are

$$\phi = \arccos\left(\frac{2h_E}{L}\right) \quad \text{and} \quad \theta = \arctan((x_t - x_r), (y_t - y_r)) \quad (36)$$

The received E_s signal is assumed to be constant in amplitude and phase between samples. The amplitude is obtained from the receive power, which is calculated from equations (34), (36), and (35). The phase is chosen randomly for the first sample and maintained constant thereafter. The E_s contribution at each element of the array is then computed by adjusting the phase, according to the element x , y position and the signal direction. This contribution which is constant over all samples, is added to the scattered signal seen by each element, to get the total received signal for that element.

3.0 DIRECTION-FINDING SYSTEM MODEL

The receiving array employed by the simulation package can have a variable number of element antennas, with arbitrary x , y positions, measured relative to the receiving reference point x_r , y_r . At the time of writing, two options exist for the receiving and transmitting element antenna patterns: an isotropic radiation pattern, and a $\cos(\text{elevation})$ pattern similar to that experienced by a short whip antenna over perfectly conducting ground.

Two techniques have been employed in the simulation package, to perform the direction-finding: a plane-wave fitting technique, and the MUSIC algorithm.

3.1 Plane-Wave Fitting Procedure

An iterative search procedure is invoked to find the best plane-wave fit to the total received signal at the array elements. The signals seen by the N element antennas can be viewed as the complex components of a N -dimensional 'signals' vector. A hypothetical plane wave would likewise have its corresponding N -dimensional array response vector which could be calculated from the plane-wave direction and amplitude. The best plane-wave fit has the minimum error power, i. e., the length of the difference vector between the plane wave response vector and the total received signal vector seen at the array elements is a minimum over all plane wave directions and amplitudes.

It can be shown that the array signals vector calculated for a unit-amplitude plane wave in a given direction will have a correlation C with the received signals vector which is a maximum when the direction is the best-fit direction. The correlation is given by

$$C = \sum_{n=1}^N s_n e^{i\delta_n} \quad (37)$$

where s_n is the complex received signal sample at the n th antenna, and δ_n the phase of the plane wave at the n th antenna, which is given in terms of the plane wave bearing α and zenith angle β , by

$$\delta_n = -\frac{2\pi}{\lambda} (x_n \sin \alpha + y_n \cos \alpha) \cos \beta, \quad (38)$$

where x_n , y_n are the antenna coordinates. The corresponding best-fit amplitude is given by

$$A = C/N \quad (39)$$

The iterative search procedure described below is used to find the best-fit plane-wave direction (i.e., bearing α and zenith angle β):

1. First, the number of sidelobes that could exist in the pattern of the array when steered to a direction are estimated, by considering the total change in phase that can occur between the furthestmost elements of the array, in going from signals parallel and antiparallel to a particular axis. These numbers, for the x and y axes correspond to the number of local maxima that can exist in the correlation function C over all directions.

2. Next a suitable number of steps in direction cosine are selected, to ensure that each sidelobe or local maximum will be seen. In the model, the number of steps n_x , n_y were set to 5 times the number of possible sidelobes, in the x and y directions. The direction cosines, in the x and y directions, are

$$\Delta_x = -\sin\alpha\cos\beta \quad \text{and} \quad \Delta_y = -\cos\alpha\cos\beta, \quad (40)$$

respectively. The direction cosines Δ_x and Δ_y are stepped from 0 to 1 in steps of $1/n_x$ and $1/n_y$, and the correlation function C evaluated for each combination of Δ_x and Δ_y .

3. The 8 largest values of C are selected, along with their direction cosines, as possible choices for an approximate maximum.
4. For each of these points, an iterative search procedure is followed, to find the local maximum. This consists of halving the step size, and computing C for Δ_x and Δ_y a step away from the present point, in both x and y directions. These new values are compared with the previous C -value, and the point corresponding to the largest value chosen. The step size is halved again, and the procedure repeated. The process is continued until the step size falls below a predetermined small value (.01). The final point and its C -value are taken as the local maximum.
5. The largest of the 8 local maxima thus found is taken as the maximum. The corresponding best-fit direction is found from the corresponding direction cosines Δ_x and Δ_y by

$$\alpha = \text{atan}(-\Delta_x, -\Delta_y), \quad \beta = \text{acos}\left(\frac{-\Delta_x}{\sin\alpha}\right) \quad \text{or} \quad \beta = \left(\frac{\Delta_y}{\cos\alpha}\right) \quad (41)$$

The corresponding complex amplitude of the best-fit plane wave is found from equation (39).

The difference between the total signal at each of the array elements and the corresponding best-fit plane wave signal is estimated. The power of this difference is summed across the antennas and compared to the total received power also summed across the antennas. The resultant error-power fraction is reported by the plane-wave-fitting program, as a 'quality factor' representative of the goodness of fit.

The plane-wave-fitting procedure requires only a single sample, and provides a single representative arrival direction as well as a plane-wave goodness-of-fit value.

3.2 MUSIC Algorithm

This section provides a brief theoretical discussion of the MUSIC algorithm [11], and a description of how it is implemented.

The signals received by the N-element array can be written as a vector $\hat{x}(t) = \begin{bmatrix} x_1(t) \\ \vdots \\ x_N(t) \end{bmatrix}$,

where (t) denotes time dependence. The covariance matrix of these signals is given by $R = \overline{\hat{x}\hat{x}^H}$, where the averaging is denoted by the overhead bar $\overline{}$, and a conjugate transpose, by the superscript H . In order to compute R , the averaging is taken over a sequence of time-samples

generated by the simulation. The normalized eigenvectors of R are denoted by $\hat{e}_1, \dots, \hat{e}_N$, arranged according to the size of their corresponding real eigenvalues $\lambda_1, \dots, \lambda_N$, in increasing order.

For S independent signals incident on the array ($S < N$), the eigenvectors $\hat{e}_{N-S+1}, \dots, \hat{e}_N$ span the signal space generated by the signals, while the remaining (orthonormal) eigenvectors span the noise space.

A unit-amplitude plane-wave signal vector $\hat{r}(\alpha, \beta)$ corresponding to a particular direction, i.e. azimuth α and zenith angle β , has the form

$$\hat{r}(\alpha, \beta) = \frac{1}{\sqrt{N}} \begin{bmatrix} e^{i\delta_1(\alpha, \beta)} \\ \vdots \\ e^{i\delta_N(\alpha, \beta)} \end{bmatrix}, \quad (42)$$

where the $\delta_n(\alpha, \beta)$ are given by equation (38). For a direction (α, β) to correspond to a signal in the signal space, its corresponding signal vector $\hat{r}(\alpha, \beta)$ must be perpendicular to the noise space. That is, its projection length onto the noise space, given by

$$\Pi(\alpha, \beta) = \left(\sum_{n=1}^{N-S'} |\hat{r}(\alpha, \beta) \hat{e}_n^H|^2 \right)^{1/2}, \quad (43)$$

is zero. In practice, a minimum will do. The MUSIC algorithm consists of making a guess at the number of 'signal' directions S' , then using the S' eigenvectors corresponding to the S' lowest eigenvalues to define the noise space (i.e., setting $S = S'$). Equations (42) and (43) are then used along with a search procedure, to finding the S' directions (α, β) corresponding to the S' lowest local minima of $\Pi(\alpha, \beta)$.

The implemented procedure for determining signal directions according to the MUSIC algorithm is as follows:

1. Find the covariance matrix R for the sequence of signal samples, and from it calculate the corresponding normalized eigenvectors $\hat{e}_1, \dots, \hat{e}_N$ arranged according to increasing eigenvalue. (The sequence length $M \geq N$ for R to be nonsingular.)
2. Specify the desired number of directions (S') to search for.
3. Searching over all directions (α, β) , compute $\Pi(\alpha, \beta)$ from (38), (42), and (43), looking for the S' lowest local minima. The search technique is conducted over the direction cosines, in a manner similar to that described in section 3.1 for the plane-wave fitting technique. The estimated signal directions are those of the S' lowest minima. The corresponding projection lengths Π are an estimate of how well each of the directions fit the signal space.

The implemented MUSIC algorithm requires a sequence of signal samples from each of the array elements, and an operator request as to the number of signal directions to look for. It provides the requested number of signal directions along with an estimate of how well each direction fits into the signal space represented by the sequence of signal samples.

4.0 TESTS OF THE FIELD-ALIGNED SCATTERING MODEL WITH PLANE-WAVE FITTING

4.1 Operational Parameters

A number of simulations were performed to examine the implications of the field-aligned scattering model, and to compare the results with those of the previously acquired Kestrel data [9,10]. These simulations used a receiving array geometry and a transmitting location similar to that of the Kestrel measurements on the Thule transmissions. The receiving array consisted of seven elements at specified locations about a circle of 25 m radius. The transmitting antenna was assumed to be 700 km distant, and the operating frequency was set to 8.0 MHz. The transmitting and receiving antenna patterns were assumed to be those of a short vertical whip on a perfectly conducting ground plane. Although these patterns do not match those of the Kestrel experiment, they do possess the overhead null of the actual antenna patterns and are sufficient to demonstrate the model. The assumed transmitted power was 1 kW, and the receiver threshold, -115 dBm.

The ionosphere was assumed to have a F-region height of maximum h_0 of 350 km, and a halfwidth y_m of 100 km. Various values were attempted for the critical frequency f_0 , from 5 to 10 MHz. Scattering region or patch sizes were 200 by 200 km. The scattering-center density inside these patches was taken as constant; values for different tests ranged from .01 to 0.1 scattering centers/km² corresponding to 400 to 4000 scattering centers per patch, respectively. The effective scattering width w_0 at the height of maximum h_0 was arbitrarily selected to be 10 m.

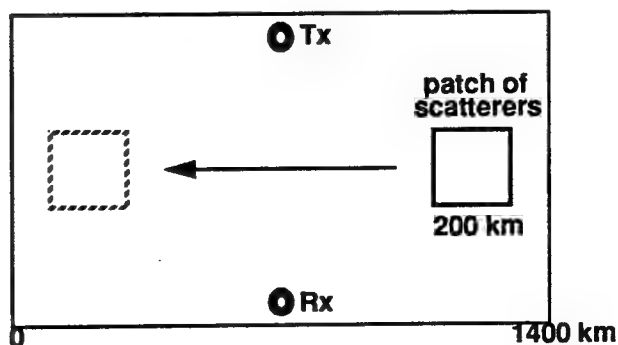
The plane-wave fitting DF technique was employed for direction estimation. This technique was similar in most respects to the technique used for the Kestrel data.

4.2 Simulation Results

4.2.1 Single Scattering Patch

A series of simulations were run, using the simple case of a single scattering patch with a horizontal motion perpendicular to the direct transmitter-receiver path (referred herein as the great-circle path, despite the flat-earth geometry), crossing the great-circle path at the midpoint. This geometry is illustrated in Figure 7. A 2-km shift of the scattering patch was used between estimates, which corresponds to a 4-second time for a drift velocity of 500 m/sec which is typical of the polar cap.

Figure 7. Plan view of single-patch scattering geometry.



In the first test, a critical frequency f_0 of 7.0 MHz was used. This corresponds to a situation where the corresponding ionospheric electron density is a little higher than the minimum needed to support propagation of the 8 MHz transmitted signal along the 700 km great-circle transmitter-receiver path. The density of scattering centers was assumed to be $.02/\text{km}^2$. The stronger of the two postulated scattering-width height dependencies (equation (29)) was used, corresponding to the excess electron density of the scatterers being proportional to the ambient electron density.

Figures 8a, b, c, and d show the results obtained. Figures 8a and b show the estimated plane-wave bearings and elevations as a function of estimate number or time. (A 0° bearing corresponds to the great-circle direction from the transmitter.) The bearings and elevations appear to follow the location of the patch of scatterers, with apparently random point-to-point variations.

The point-to-point bearing variations cover a range of values roughly equal to the bearing angle subtended by the patch at the receiving array, at any one time. The elevation variations, on the other hand, are substantially less than the elevation angle subtended. For instance, at the midpoint of the simulation when the patch is halfway between the transmitter and receiver, it subtends a bearing angle of 33° centered on 0° , and at the height of maximum electron density, an elevation angle of 17° centered on 45° . An inspection of Figures 8a and b for this time indicate a similar bearing spread for the direction estimates, but a much smaller elevation angle spread. The elevation angles with a few exceptions lie within a 5° range centered on 43° . This is likely due to the fact that the strongest contributions to the signal come from those scattering centers which intersect the generally better-focused low-angle ray nearest the height of maximum electron density. This is a result of the larger scattering cross section as well as the increased focusing that occurs for low-angle rays which approach those heights. These scattering centers are located in the patch along the bisector of the transmit-receive great-circle path, where the elevation angles for scatter propagation are expected to lie in a narrow range near 45° .

Figure 8c shows the estimated signal directions obtained in the run, in an elevation-versus-bearing plot. The directions are scattered about a well-defined arc centered on the great-circle (0°) bearing. This behaviour is expected, since ray paths closer to the great-circle path will by virtue of their shorter distances correspond to higher elevation angles which penetrate higher into the ionosphere.

Figure 8d is a time history of the number of scattering points, or propagation paths contributing to the signal seen by the array. With the specified density of scattering centers ($.02/\text{km}^2$) and the scattering patch size (200 km square), there are 800 scattering centers, each possibly contributing a high-angle and a low-angle ray to the signal. For most of the time, the number of scattering points in Figure 8d is slightly less than 800. This implies that only the stronger low-angle rays contributed to the signal. The high-angle rays for most scatterers had near-zero zenith angles for which the defocusing was very high, and so were rejected by the simulation program. At the midpoint of the run, the number of contributing paths rises slightly above 800. The patch is midway between the transmitter and receiver at this time, so that the 7.0 MHz transmitter frequency was closer to the MUF (maximum useable frequency) for the scatter propagation paths. The high-angle ray under these circumstances would not lie as close to the zenith, so that its contribution would be included.

The resultant signals were observed to fit a single plane wave remarkably well. Of the 500 estimates represented in Figures 8a, b, c, and d, 398 had an error power fraction (Section 3.1) of less than or equal to 0.1. In other words, for 398 out of 500 estimates, 90 percent or more of the received signal power could be attributed to a single plane wave.

Figure 8a. Estimated plane-wave bearing, as a function of estimate number, for the single-patch geometry of Figure 7 and a critical frequency of 7 MHz.

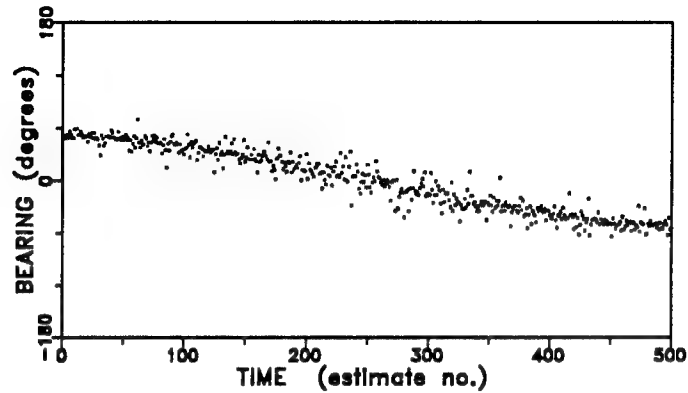


Figure 8b. Estimated plane-wave elevation, as a function of estimate number.

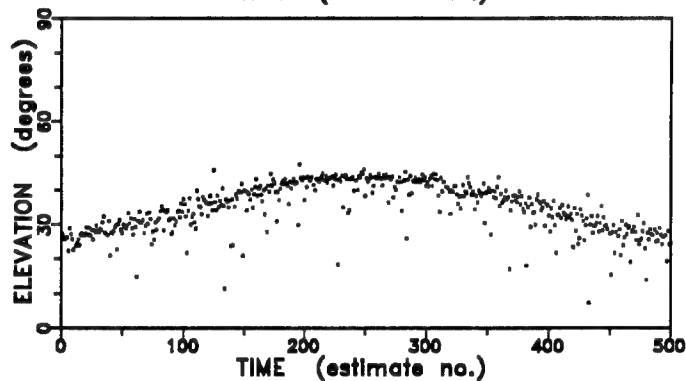


Figure 8c. Estimated plane-wave directions, plotted in terms of bearing and elevation.

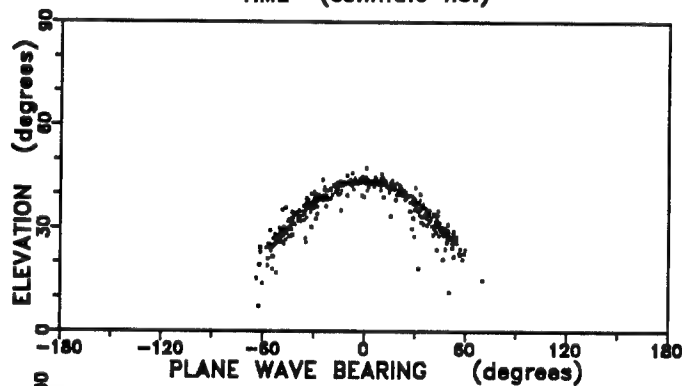
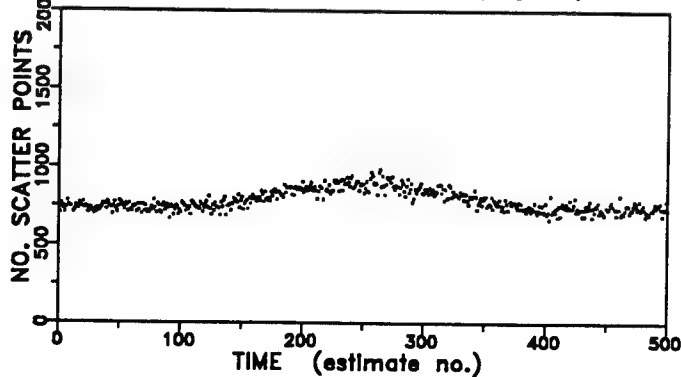


Figure 8d. Number of propagation paths contributing to the signal, as a function of estimate number.



4.2.1.1 Dependence on Ionospheric Electron Density

The ionospheric electron density is specified in terms of the critical frequency f_0 , and determines the maximum frequency (MUF) that will propagate between any two points a specified ground distance apart. In testing the model, f_0 was varied to obtain great-circle MUFs that were a little greater than, nearly equal to, and less than, the transmitting frequency f . These values of f_0 were 7.0, 6.5, and 6.0 MHz respectively. The geometry was that of Figure 7, and the remaining ionospheric and scattering parameters, the same as previously used. The results are shown in Figures 9 and 10.

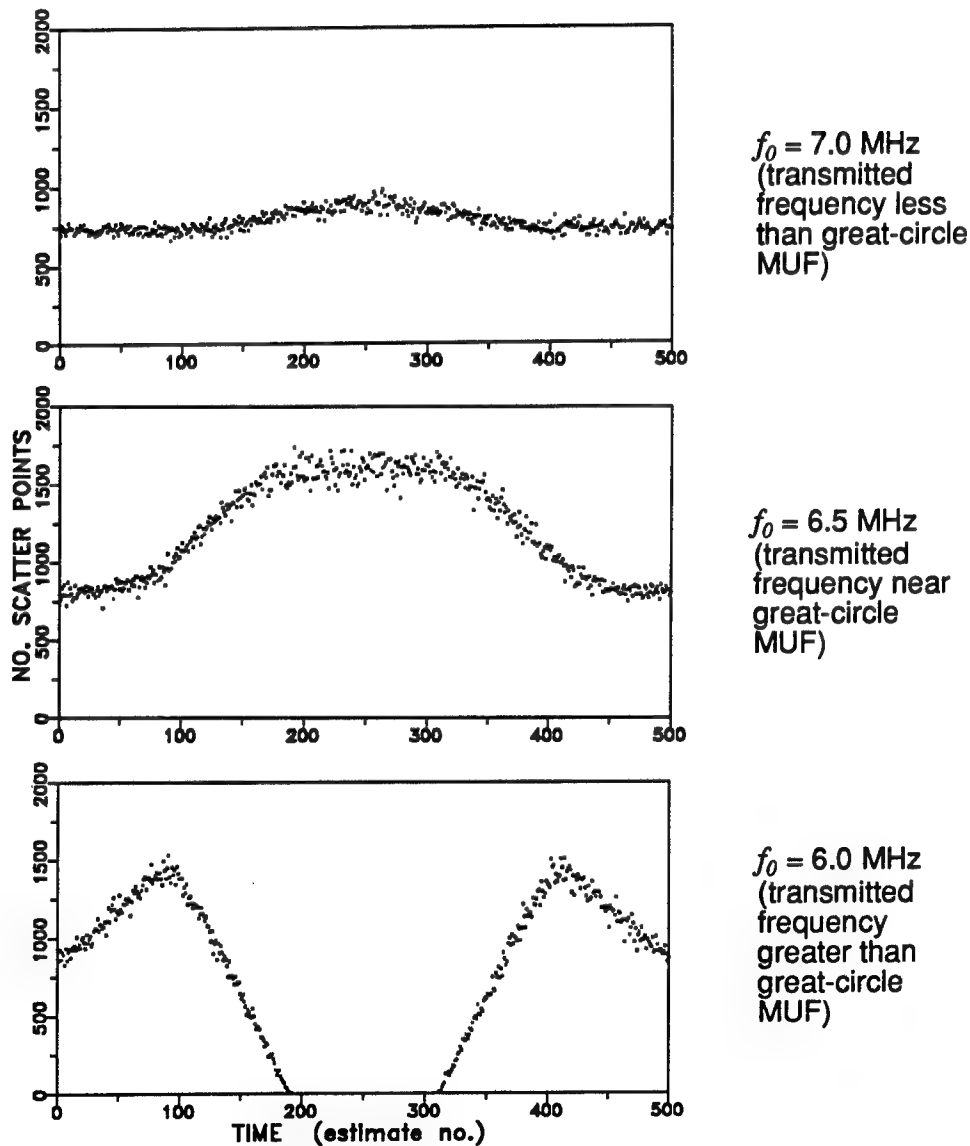
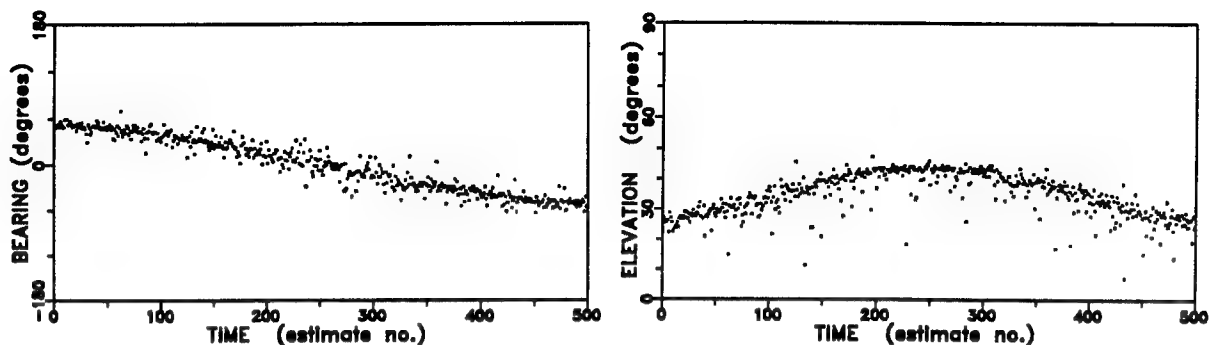
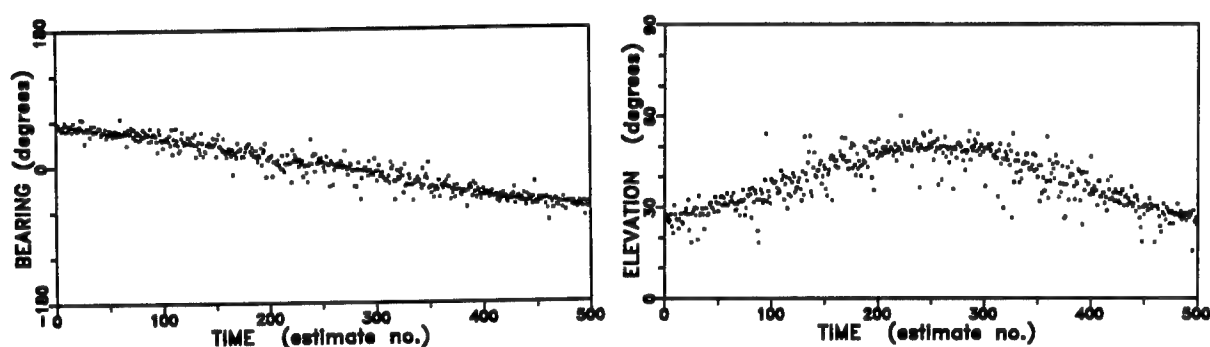


Figure 9. Number of contributing paths, as a function of estimate number, for the single-patch geometry of Figure 7 and various critical frequencies f_0 .

$f_0 = 7.0$ MHz (transmitted frequency less than great-circle MUF)



$f_0 = 6.5$ MHz (transmitted frequency near great-circle MUF)



$f_0 = 6.0$ MHz (transmitted frequency greater than great-circle MUF)

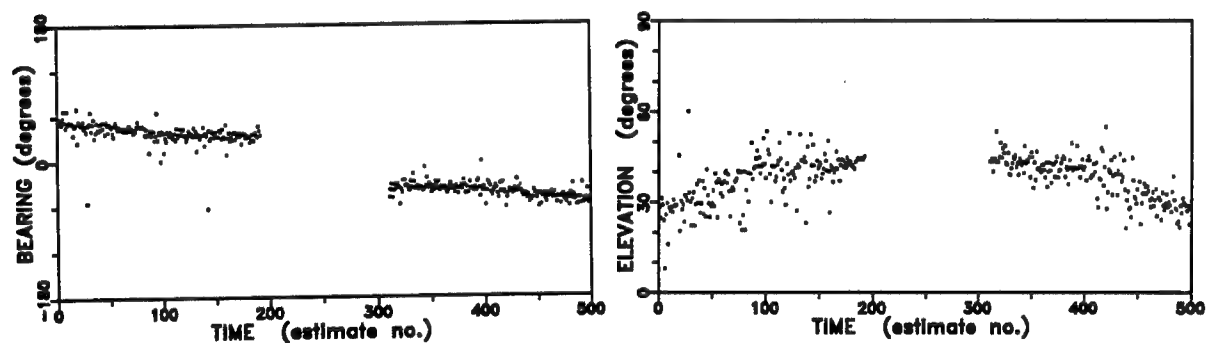


Figure 10. Estimated plane-wave bearing and elevation, as a function of estimate number, for the single-patch geometry of Figure 7 and various critical frequencies f_0 .

Figure 9 shows the number of scatter points or paths contributing to the signal, as the patch moves from right to left of the transmitter-receiver great-circle path, for the three critical frequencies f_0 .

The behaviour for $f_0 = 7.0$ MHz has already been discussed. In this case, the MUF for the great-circle path is above the transmitted frequency so propagation over this path is supported.

At $f_0 = 6.5$ MHz, the MUF for the great-circle path drops close to the 8.0 MHz transmitted frequency, so that the number of contributing paths begins to depend strongly on patch position. At the start and end of the simulation the patch is well removed from the great circle so that the scattering path lengths are much longer and the MUFs well above 8.0 MHz. The number of contributing paths is near 800, corresponding to one path per scattering center (the low-angle path). The high-angle paths are dropped as a result of their being very close to the zenith and thus extremely defocused. As the patch approaches the great circle, the MUFs for the scattering paths drop toward the transmitted frequency. The zenith angles for the high-angle paths increase, and they begin to be included in the signal estimation. The number of paths seen near the midpoint of the run is approximately 1600 as a result of both the low and high-angle paths of all scattering centers in the patch contributing to the signal.

At $f_0 = 6.0$ MHz, the great-circle-path MUF has dropped below the 8.0 MHz transmitted frequency and the behaviour is radically different. Propagation becomes impossible for those scattering centers whose horizontal path length corresponds to a MUF below 8.0 MHz. Thus the number of contributing paths drops as the patch approaches the great circle, from 1600 to zero.

The corresponding bearing and elevation behaviour is shown in Figure 10.

As the critical frequency is dropped from 7.0 to 6.5 MHz, there is little change in the estimated bearings. A noticeable increase is seen in the estimated elevation angles, especially when the patch approaches the great circle. This is due to the added contribution of the high-angle rays to the signal as well as the increased elevation angles for the low-angle rays which are able to penetrate further into the less dense ionosphere.

When the critical frequency drops to 6.0 MHz, below that needed to support great-circle-path propagation, there is a significant change in the estimated bearings. There are no bearing estimates for the times where the patch is sufficiently close to the great circle that none of the scattering distances support propagation. For slightly farther patch positions, the bearings reflect the positions of the farthest scattering centers in the patch, whose horizontal propagation paths are long enough to support propagation. When the patch is sufficiently distant from the great circle, all scattering centers support propagation and the bearings are centered roughly toward the midpoint of the patch.

A different aspect of the influence of the ionosphere on scattering propagation is seen when a critical frequency well above the great-circle-path MUF is used. Figures 11a, b, and c show the time history for a critical frequency of 10.0 MHz. Other model parameters are identical to those used previously.

Figure 11a shows the number of scattering paths contributing to the signal as a function of time, as the patch moves from right to left of the great circle. The number (~ 300) is well below the number of scattering centers (~ 800) in the patch, and remains so over the path of travel of the patch. This happens because the portion of the propagation path lying inside the ionosphere is quite short when the transmitted frequency is well below the MUF. A scattering center contributes to the propagation only when its propagation paths intersect it at a point inside the ionosphere. The region where the potential paths lie inside the ionosphere at the point of scattering is in this case a narrow strip which crosses the great-circle path perpendicularly at its midpoint. Only the scattering centers inside this region can contribute to the signal. The number of contributing paths at the midpoint (~ 270) suggest that this region is roughly $270/800 \times 200 \text{ km} = 67.5 \text{ km}$ wide at the point where it crosses the great circle.

Figure 11a. Number of propagation paths contributing to the signal, as a function of estimate number, for the single-patch case of Figure 7 and a critical frequency of 10 MHz.

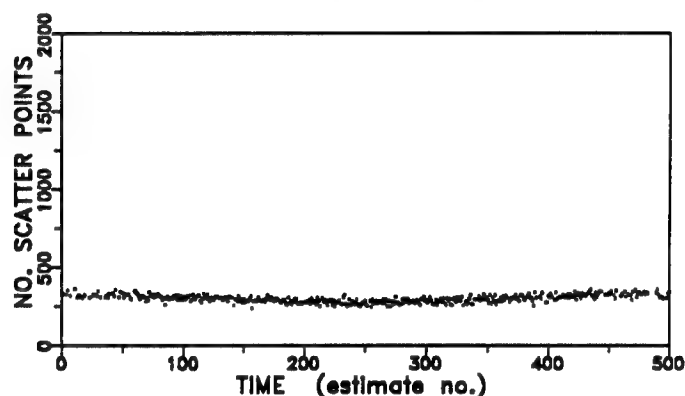


Figure 11b. Estimated plane-wave bearing, as a function of estimate number, for a critical frequency of 10 MHz.

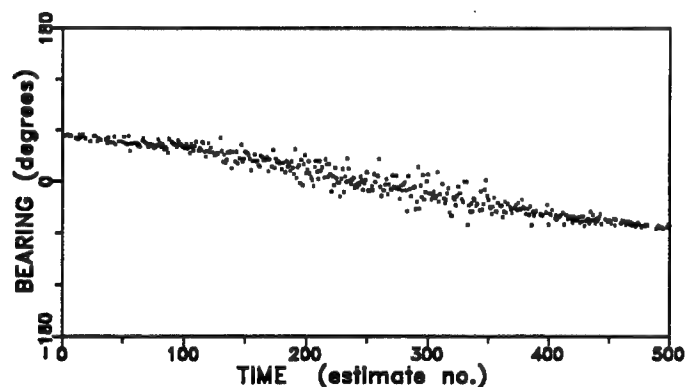
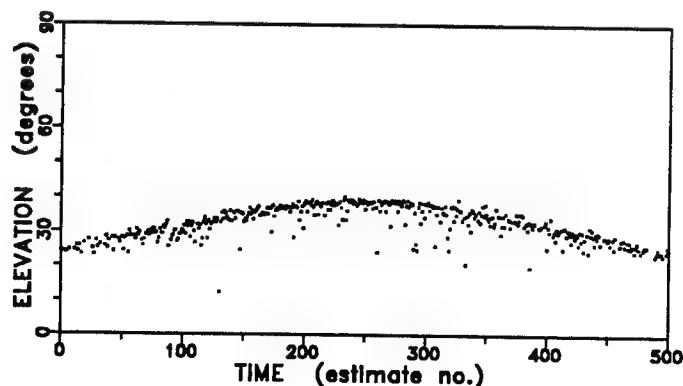


Figure 11c. Estimated plane-wave elevation, as a function of estimate number, for a critical frequency of 10 MHz.



Figures 11b and c show the bearing and elevation time histories respectively for $f_0 = 10.0$

MHz. The most prominent difference between these figures and the earlier ones for 7.0 MHz (Figure 8a and b), is the reduced point-to-point scattering in the estimated bearings at the start and end of the run. This is explained by the narrowness of the strip wherein scattering centers can contribute to the signal. The intersection of this strip with the scattering patch at the start and end of the run subtends a smaller bearing angle at the receive array, giving rise to the smaller spread in estimated bearings. Another difference is in the elevation angles, which for any particular time are lower than those found with a 7.0 MHz critical frequency. These elevation angles are lower since with a higher critical frequency the paths do not penetrate as deeply into the ionosphere.

4.2.2 Effective Scattering Region

From the previous discussion for the 10.0 MHz critical frequency, it is evident that the scattering centers which are capable of contributing to the signal are, by virtue of the height at which they intersect the propagation path, limited to a narrow region which is centered on the perpendicular bisector of the great-circle transmit-receive path. Equation 17, which gives the propagation distance D as a function of the zenith angle ϕ_0 , was used to calculate the boundaries of this region, as described below.

In order to calculate the locations of these boundaries, a computer program was written which takes as input the ionospheric parameters: height of maximum h_0 , half-width y_m , and critical frequency f_0 ; the transmitter and receiver (X, Y) coordinates, and the operating frequency f .

In the program, the (X, Y) coordinate system is chosen so that the transmitter and receiver lie along the y -axis, with the origin at the halfway point (See Figure 12). The perpendicular bisector to the great-circle transmit-receive path is then the X -axis, i.e., the equation $Y = 0$. The program steps the X -value over the range of values desired for plotting. The corresponding y -coordinate of the lower boundary to the effective-scattering-region strip is found for a particular X , by a search procedure which involves decreasing Y from zero, in steps. For each point (X, Y) , the program computes the geometric distance D' and compares it to the distance D found using equation (17). The horizontal path length D' expected from the geometry is calculated from the (X, Y) location in question, together with the transmit and receive locations. A zenith angle is obtained by using the boundary condition

$$\phi_0 = \text{atan} \left(\frac{h_0 - y_m}{d_1} \right) \quad (44)$$

where d_1 is the geometric ground distance between the scatter and receive locations. The propagation distance D corresponding to ϕ_0 is then computed from (17) and compared with the geometrically obtained value D' . Initially, at $y = 0$, D will be greater than D' . As Y becomes more negative, D becomes less, and eventually drops below D' . When this happens, the two most recent values are interpolated to determine the point at which $D = D'$. This corresponds to the minimum value Y_{min} . The maximum value, by symmetry is given by $Y_{max} = -Y_{min}$. For some critical frequencies and X -values, as Y is made more negative, the ray will begin to penetrate right through the ionosphere before D (found from (44) and (17)) drops as low as the geometric distance D' . This situation corresponds to the geometric distance D' being inside the skip range so

that propagation is impossible. The penetration condition was checked for at each step in the program, by invoking equation (19). In this way, the boundaries of the strip of allowed scattering locations are found for plotting.

Figure 12 is the resulting plot of the boundaries of the strip within which scattering centers are capable of contributing to the signal at the receiving array. The minimum and maximum values of y are plotted as a function of x , for several values of critical frequency f_0 . The transmit-receive geometry and ionospheric parameters are the same as used previously.

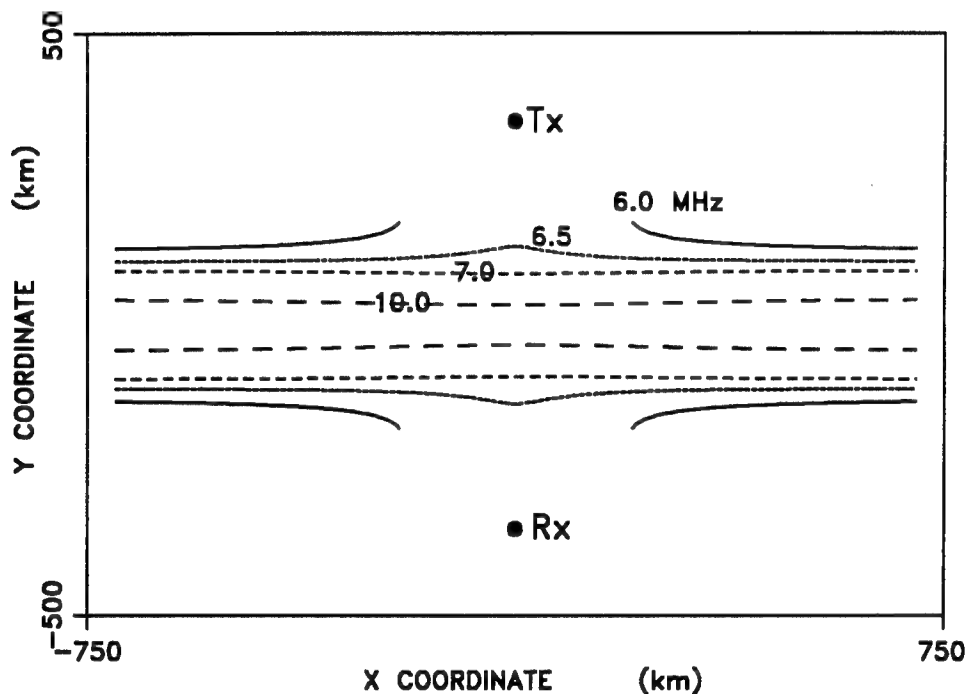


Figure 12. Boundaries of the allowed region wherein scattering centers can contribute to the signal seen at the receiving array, for various critical frequencies.

Several things are apparent from this figure. The width (i.e., y -extent) of the allowed region, when the critical frequency is less than that needed to support great-circle propagation (e.g., 6.0 MHz), increases as one moves closer to the great circle, up to a point where the rays begin to penetrate through the ionosphere making propagation to the receiver impossible. There is also a slight widening near the great circle, for critical frequencies just above that needed to support great-circle propagation (6.5 MHz). However, as the critical frequency increases further, an opposite effect occurs. At a critical frequency of 10.0 MHz, the width of the allowed region decreases slightly as the great circle is approached.

The width of the allowed region where it crosses the great circle is seen from Figure 12 to be 68 km, for a critical frequency of 10.0 MHz. This is in good agreement with the 67.5 km width inferred from the number of contributing scattering centers (Section 4.2.1.1).

4.2.3 Variation of Scattering Efficiency with Height

The simulations of Section 4.2.1 which were performed using the stronger scattering-width height dependence given by equation (29) were repeated for the weaker dependence given by equation (30), based upon an excess scatterer electron density proportional to the square root of the ambient electron density ($\delta N \propto \sqrt{N}$). The results were found to be essentially the same as for the stronger height dependence for which $\delta N \propto N$. However, small differences existed.

There is a tendency for the mean elevation of the direction estimates to be lower when the scattering efficiency varies less with height ($\delta N \propto \sqrt{N}$), which is expected since the higher angle rays which intersect their corresponding scattering center higher in the ionosphere would not be as strongly favoured with this height dependence. For the same reason, there is also a tendency for the rms spread in the elevation angles experienced at any one patch position to be slightly greater for the reduced height dependence. It should be emphasized that these differences are small, so that the actual form of the scattering-width height dependence plays only a small role in determining the behaviour of the field-aligned scattering model.

Further simulations presented in this paper use the weaker (equation (30)) height dependence for the effective scattering width.

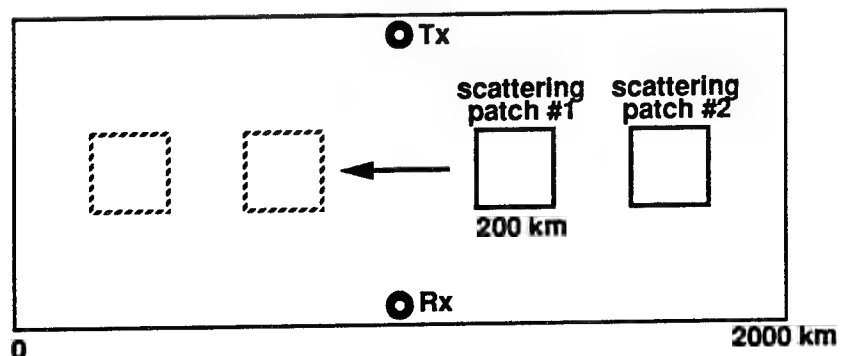
4.2.4 Multiple-Patch Case

In any real high-latitude propagation situation where there are ionospheric gradients and small-scale irregularities present as a result of the gradient-drift mechanism, the small-scale irregularities will be grouped into specific regions or patches in the vicinity of the gradients. Further, with the large-scale irregularities likely to exist at polar latitudes (e.g., Figure 1) there will likely be more than one region of high gradient present, and therefore more than one scattering patch present. The number of patches actually observed will depend on their position relative to the transmitter and receiving array, as well as the propagation conditions.

As an initial approach to multiple-patch simulation two patches are considered, each 200 km square, with similar scattering and ionospheric parameters. The ionospheric parameters assumed are given in Section 4.1, and are similar to those used for the single patch case (Section 4.2.1).

A plan view of the geometry used for many of the simulations is given in Figure 13.

Figure 13. Plan view of modelled two-patch geometry.



4.2.4.1 Initial Simulations

The initial simulations used a critical frequency of 6.5 MHz, just above the minimum required for great-circle-path propagation. A scattering-center density of $0.01 \text{ centers/km}^2$ was used, so that on average there were 400 scattering centers in each patch.

Figure 14 shows the time history of the estimated plane-wave direction, described in terms of bearing and elevation. As the simulation run progressed, the observed bearings in Figure 14 are directed mostly toward the nearer patch, first directed to patch #1, then to patch #2. A separate analysis of two plane-wave signals shows that a plane-wave estimator will be always directed primarily toward the stronger signal, provided it is 1 or more dB above the weaker one. For much of the time, the observed bearing jumps between the two patches, suggesting that the composite signals from the patches vary randomly in amplitude so that sometimes one patch has the stronger signal, sometimes the other. The corresponding elevation time history in Figure 14 appears to be the composite of two arcs, each peaking near the time their implied patch crosses the great circle. Near the middle of the run, the observed elevations appear to jump between the implied arc for one patch, and the arc for the other.

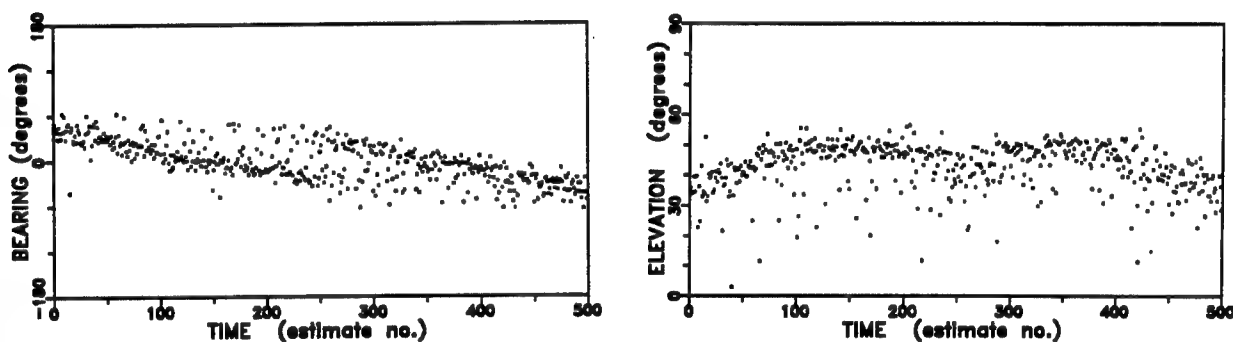


Figure 14. Time histories of estimated plane wave bearing and elevation, for the two-patch geometry of Figure 13, with a critical frequency of 6.5 MHz and a scattering-center density of $0.01/\text{km}^2$.

It may be thought that the degree of randomness in the composite signal coming from a single patch, and therefore the uncertainty as to which patch contributes the stronger signal thus capturing the plane-wave direction, is a result of the small number of scattering centers used (an average of 400 per patch). To see if this is the case, the scattering-center density was increased tenfold, to $0.1/\text{km}^2$, (4000 scattering centers per patch) and the simulation repeated. No dramatic change was seen in the estimated plane-wave direction histories when the scattering-center density was increased tenfold. The duration of time where both patches were seen, i.e., where the estimated plane-wave direction jumped back and forth between the general directions of the two patches was roughly the same for the two densities.

4.2.4.2 Dependence on Ionospheric Electron Density

In order to illustrate the strong role played by ionospheric refraction in the scattering model, and the degree of complexity that can result in a direction-finding record when more than one scattering patch is present, tests were run using various critical frequencies both above and below that needed to support great-circle propagation. The geometry of Figure 13 was used for these tests, along with a scattering-center density of $0.02/\text{km}^2$. The resultant bearing and elevation histories are shown in Figure 15.

For a critical frequency f_0 of 5.0 MHz, propagation is not supported for scattering-center positions within 440 km of the great circle, represented by 0° bearing.. At the start of the run, only the scattering centers in the furthest patch (#2) contribute to the signal, and when this patch moves closer than 440 km, the signal disappears altogether, near estimate 180. Up to that time, the bearing and elevation estimates of Figure 15 reflect the location of the patch #2 scatterers which contribute to the signal. For estimates 180 to 320, there is no propagation for scattering centers from either patch, and thus no signal. After estimate 320, patch #1 moves past 440 km on the other side of the great circle, and scattering centers from that path begin to contribute to a signal. The plane-wave estimates for the signal reflect the scattering positions within patch #1 that are more than 440 km from the great circle. Thus, for a 5.0 MHz critical frequency, only the further of the two patches is seen, and for only part of the time, owing to the large skip distance imposed by the ionosphere.

At $f_0 = 6.0$ MHz, propagation is not supported for scattering positions within 100 km of the great circle. At the beginning of the 6.0 MHz run, signals from both patches are present, and the resultant bearings and elevations of Figure 15 are directed toward the nearer patch (#1). After the first 80 estimates, the patches move so that some scattering centers inside patch #1 are closer than 100 km from the great circle and do not contribute to its signal. At this point the estimated plane-wave signal direction switches to patch #2 which now has the stronger contribution. The estimated directions continue to follow the locations of those scattering centers inside patch 2 which remain outside 100 km of the great circle. Patch #1 crosses the great circle and begins to move outside the 100-km limit on the other side of the great circle. Patch #1 begins to again contribute to the signal, while patch #2 which is now moving inside the 100-km limit on the other side of the great-circle begins to have its contribution reduced. For a period (estimates 220 to 280), the contributions of both patches are fairly close in mean power, so that random fluctuations cause the resultant plane-wave direction to jump back and forth between the positions of the contributing scattering centers in each patch. After estimate 280, patch #2 moves completely inside the 100-km limit and patch #1, outside the 100-km limit on the other side. The direction estimates reflect the location of patch #1 at this point. This continues until patch #2 crosses the great circle and moves outside the 100-km limit, whereupon it, as the nearer of the two patches, begins to control the estimated plane-wave direction (after estimate 410).

At $f_0 = 6.5$ MHz, propagation is supported for all scattering locations. The estimated plane-wave directions are controlled by the patch that has the stronger composite signal. This depends not only on the number of scattering centers in the patch, but also the effective scattering width for each scattering center (and hence the height of scattering), and the ionospheric focusing that occurs for that path. In addition, the geometric path loss involved also favours the shorter paths.

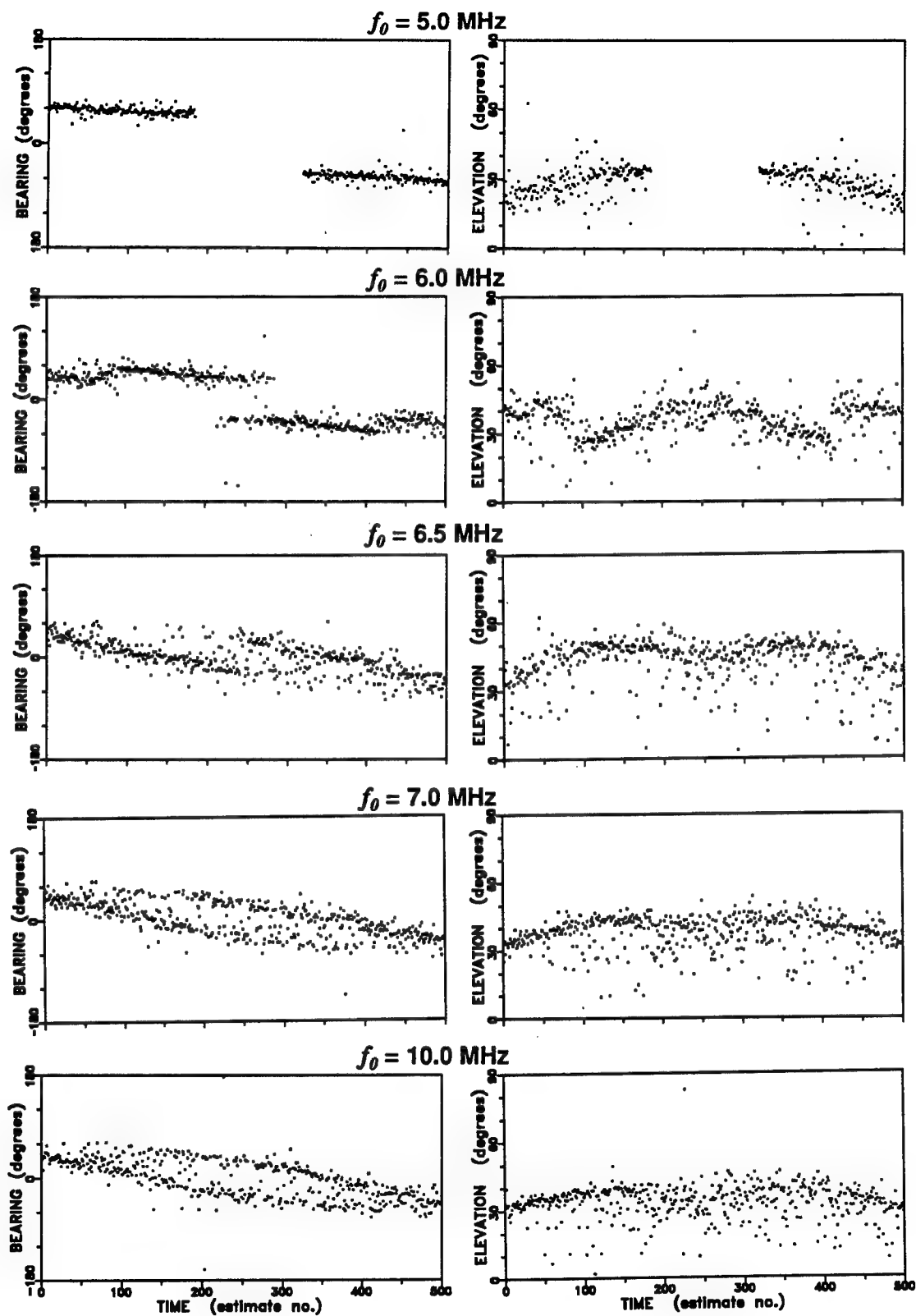


Figure 15. Estimated plane-wave bearing and elevation time histories for the two-patch geometry of Figure 13, for various critical frequencies, and an 8.0 MHz transmitted frequency.

At the start and end of the run illustrated in Figure 15, the estimated plane-wave directions are directed toward the closer of the two patches. There is a long period in the middle of the run where the estimate direction moves between the two patches, due to random fluctuations in the roughly equal signal powers now favouring one patch, then the other.

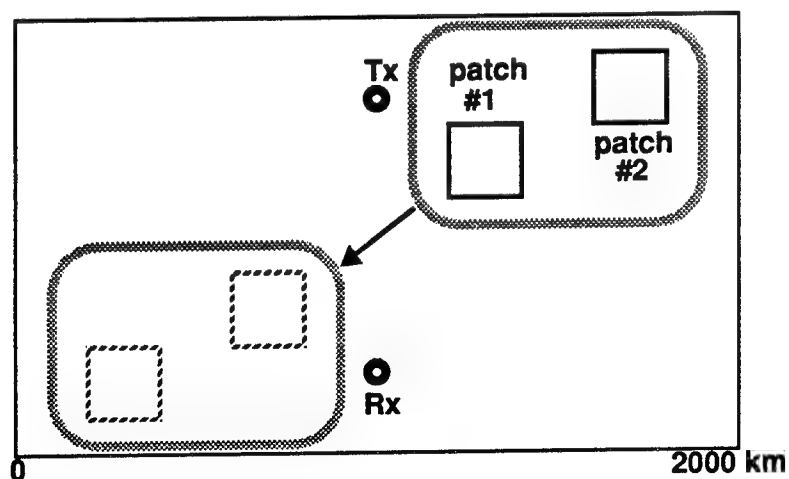
As f_0 is increased to 7.0 and then 10.0 MHz in Figure 15, the observed directions continue to favour the closer patch. However, the range of times over which both patches can be seen increases, suggesting that the composite powers from each patch are more nearly equal for a wider range of positions than previously. The main difference between the results for these critical frequencies and those of the 6.5 MHz critical frequency is the absence of those the strong ionospheric focusing that occurs for the midpoint paths near great circle whose ground distance is close to that of the skip distance. This weakening of the ionospheric focusing effect clearly reduces the dependence of the composite signal strength upon patch location.

4.2.5 Effect of Different Geometries

The geometries modelled so far have been restricted to patches moving along the perpendicular bisector of the great-circle path. This is generally not the case, and, as shown in Section 4.2.2, the perpendicular bisector occupies a privileged position at the midpoint of the allowed scattering region. It is therefore enlightening to consider other geometries.

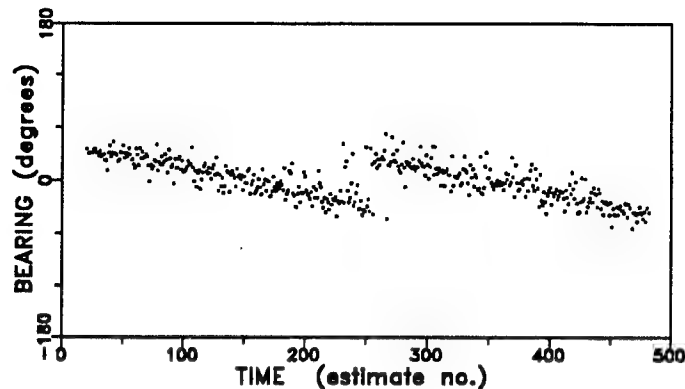
Figure 16 shows a modelled geometry where two scattering patches follow one another across the midpoint of the great-circle path, in a direction that is 26.5° off the perpendicular bisector, corresponding to a 2-km shift in x and 1-km shift in y between estimates. A critical frequency of 10.0 MHz was used for this test, along with a scattering-center density of $0.02/\text{km}^2$. The resultant bearing and elevation history is shown in Figure 17.

Figure 16. Plan view of two-patch geometry used in obtaining Figure 17.



When the bearing time history of Figure 17 is compared with that of Figure 15 for a critical frequency f_0 of 10.0 MHz, large differences are seen although the change in geometry is not great. The bearing estimates in Figure 17 switch quite abruptly from one patch to the other near

Figure 17. Time history of estimated plane-wave bearing for $f_0 = 10$ MHz, for the geometry of Figure 16.



the midpoint of the run, while those in Figure 15 jump between patches, allowing both patches to be seen at the same time over most of the run. The abrupt change in Figure 17 can be related to the scattering requirement that the scattering-center locations in order to intersect the propagation paths inside the ionosphere must lie within a narrow strip centered on the perpendicular bisector of the great-circle path, as illustrated in Figure 12. Thus, for the geometry of Figure 16, each patch is seen in turn as it intersects the strip, and only for a brief time near the middle of the run are both patches seen simultaneously.

As further influence of the effect of a changing drift-motion direction, the situation of two patches following one another along a patch crossing the midpoint of the great-circle path at 63.5° off the perpendicular was modelled, corresponding to a 1 km shift in x and 2 km shift in y between estimates. A lower critical frequency f_0 , of 7.0 MHz was used. For this frequency, Figure 12 shows a wider strip of permissible scattering locations as the rays penetrate further into the ionosphere. Figure 18 illustrates the geometry, and Figure 19 shows the resultant time history of estimated plane-wave bearings.

Figure 18. Plan view of two-patch geometry used in Figure 19.

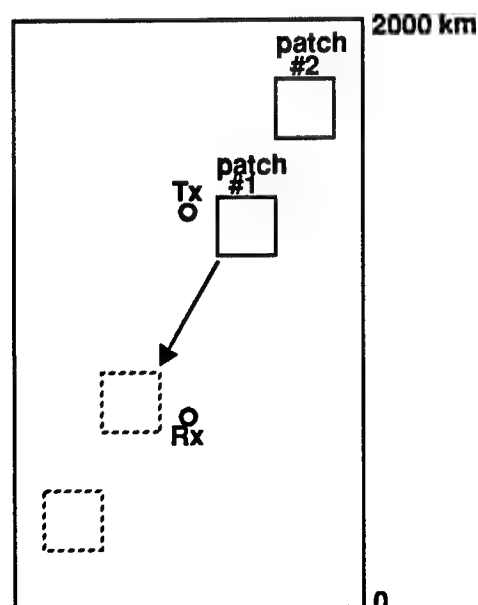
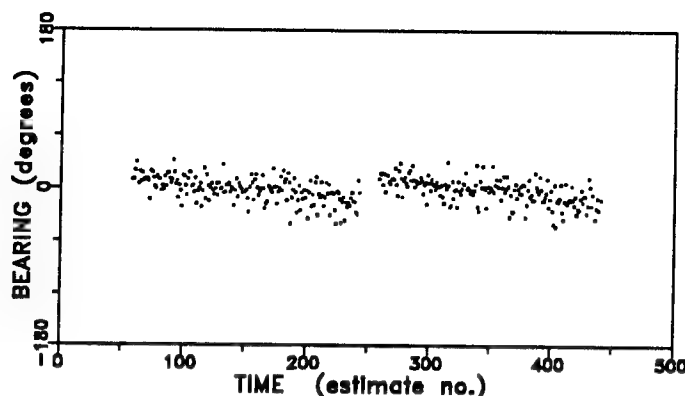


Figure 19. Time of estimated plane-wave bearings for $f_0 = 7$ MHz, for the geometry of Figure 18.



As in the previous case the estimated directions follow one patch then the other, as they pass over the strip of allowed scattering locations. As seen in Figure 19, there is a time in the middle of the run when the two patches are on either side of the strip so that neither patch is seen, and at the start and end of the run the two patches cannot be seen, as they are to one side of the strip.

4.3 Summary and Discussion of Findings

The scattering model was found to produce a composite received signal at the array that fit a plane wave surprisingly well most of the time, although the constituent signal contributions arrived from many directions from different scattering centers. When the model is run a number of times under the same conditions, the estimated plane-wave directions are distributed in direction so as to reflect the spread in direction of the constituent signals from the contributing scattering centers.

In general, the spread in bearing for a square patch of scattering centers is much larger than the spread in elevation. The spreads depend not only on the actual positions of the scatterers in the patch relative to the receive array, but also on the propagation conditions which determine the height of scattering, and the scattering locations for which propagation is possible (Figures 10, 11). The observations are not strongly dependent on the form of the height dependence of the scattering cross section.

For the horizontally stratified ionosphere modelled, the scattering centers that can contribute to the received signal are restricted to a strip of varying width, centered about the perpendicular bisector of the great-circle transmit-receive path (Figure 12). The width of this strip for ionospheric densities well above that needed to support great-circle propagation is quite narrow, less than the dimensions anticipated for many patches of scatterers. As the ionospheric electron density becomes less, the strip widens, until the point is reached where great-circle propagation is no longer supported, whereupon it splits in two. The scatterers contributing to the signal at any time are located in the intersection of the patches present with the allowed regions (as defined by the ionospheric conditions) for the scatterers to contribute. For a non-horizontally stratified ionosphere, the shape of the allowed region will be more complex than a simple strip, and will depend strongly on the ionospheric contouring present.

In the case of two or more patches of scatterers, the patch which has the strongest composite signal at the receiving array will control the estimated plane-wave direction. The present model assumes that the scatterers are regenerated randomly between consecutive estimates, based upon the short lifetimes expected for small field-aligned irregularities. As a result, the resultant composite signal for any one patch will fluctuate substantially in its strength, from estimate to estimate. When conditions are such that two patches produce signals which are fairly close in their mean power, the estimated plane-wave direction will jump from one patch to the other. Depending on the geometry and propagation conditions, two or more patches may be seen together in this way for some time (Figure 15, 7 and 10 MHz).

When the ionospheric electron density is lower than that needed for great-circle propagation, scatterers along the great-circle will not contribute to the observed signal, but others further away will contribute, provided they lie inside the allowed region. Patches of scatterers moving through the transmitter receiver path will thus cause the time history of received signal directions to be quite complex, and highly dependent of the ionospheric propagation cutoff and the geometry of the transmitter and receiver with respect to the patches and their motion (Figure 15, 5 and 6 MHz, Figures 17 and 19).

5.0 TESTS OF THE MUSIC ALGORITHM APPLIED TO THE FIELD-ALIGNED SCATTER MODEL

In considering the implications of aspect-sensitive scattering upon direction-finding, the propagation model and the DF technique cannot be viewed in isolation, but need to be treated together. In the previous section, the implications of the aspect-sensitive scattering model for direction-finding were reviewed, for the case of a plane-wave fitting (i.e., interferometric) DF technique. Those results are useful in establishing not only the effects of the propagation model (i.e. scattering and ionospheric refraction) but also the way these effects are seen by the DF system, when a plane-wave technique is employed. Such results lend themselves to comparisons with real data obtained by systems using interferometric techniques, such as that gathered by the Kestrel experiment [9,10].

In the present section, the implications of scattering upon direction finding are extended to a class of direction-finding algorithms of which the MUSIC algorithm is representative. These algorithms are coming into use in sampled-aperture systems, and are capable of obtaining a number of signal directions simultaneously. The signal directions can represent different transmissions, or a number of coexisting propagation paths for the same transmission. These algorithms consider a small number of directions, less than the number of antennas in the receiving array, so that the number of propagation paths which can be exactly identified is limited. In the case of scattering, we are dealing with a large number of paths, many more than can be specified. How the MUSIC algorithm will respond to this situation needs to be determined.

5.1 Single Scattering Patch

5.1.1 Test Parameters

Initial tests with the MUSIC algorithm deal with a single scattering patch. The geometry and ionospheric parameters are the same as those previously used (Sections 4.1, 4.2.1, and Figure 7). The effective scattering-width dependence on height is assumed to be proportional to the ionospheric electron density, as given by equation (30).

The MUSIC algorithm requires a series of signal samples to be taken for each direction estimate. In the present tests, 50 samples were generated for this purpose, for each estimate. The samples were taken 2 ms apart, and a 20-Hz Doppler spread was assumed for the signal from each scattering center (Section 2.6.3).

Consecutive direction estimates were made with a 4 km shift in the patch position between estimates. This is equivalent to an estimate every 8 seconds for the 500m/sec patch motion typical of polar-cap ionospheric convection.

5.1.2 Simulation Results

Figure 20 presents the simulation results. Time histories of the estimated bearings and elevations, found for the single-patch case using the MUSIC algorithm, are presented, for several settings of the MUSIC algorithm, i.e., different numbers of assumed signal directions. These results may be compared with those of Figure 8a and b of Section 4.2.1, obtained for the same geometry and ionospheric conditions using plane-wave fitting.

The results found with MUSIC depend strongly on the number of assumed signal directions.

From Figure 20, when a single direction is assumed, the resultant direction estimates tend to follow the central portion of the patch. There is some random scatter in the point-to-point estimates, but not so much that the directions can be said to come from anywhere in the patch. The spread in directions is much less than the angle subtended by the patch, in contrast to the result found with the plane-wave fitting procedure in Figures 8a and b, where the spread was more representative of patch size.

When two signal directions are assumed, the estimated directions of Figure 20 tend to represent the two sides of the patch as seen at the receiving array. There are, in effect two traces, on the bearing and elevation time history plots, representing the two sides. At the start of the run, the lower trace on the bearing plot represents the side of the patch nearest to the great-circle, and corresponds to the elevation trace with the higher elevation. Each side is associated with a bearing trace that becomes lower with time, and an elevation trace that increases up to the point where the side crosses the great-circle transmit-receive path after which it decreases. The separation of the two bearing traces is representative of the angle subtended by the patch at the receiver. However the two traces would appear to suggest two smaller patches rather than a single extended patch.

In addition to the two traces representing the edges of the patch, there are several shorter traces that appear during the run, which bear no clear relationship to the patch position, and which have relatively fixed azimuths. There are two likely causes for these extra traces. One possibility is due to the large sidelobes which are beginning to appear in the receiving array pattern at the 8 MHz operating frequency. Directions of sidelobes whose amplitude is close to that of the main lobe may be identified as signal directions whenever the actual signal coming from a large number of other directions is sufficiently nonplanar. The second possibility is an artifact of the search procedure employed for finding the signal directions, which may occasionally cause certain boundary points of the direction cosines searched to be identified as signal directions.

When the number of assumed signal directions is increased to three and then to four, the direction estimates tend to fill in the area between the two traces found for the two-direction estimation. The fact that the signals come from a single extended patch becomes fairly clear. The direction estimates cover a region whose extent is representative of the angle subtended by the patch at the receiving array. Further, the subtended angle is much better defined in these cases than it is for the plane-wave-fitting result in Figures 8a and b. At the same time, the extra traces possibly arising from array sidelobe effects and algorithm artifacts become much stronger, enough so that measures to remove them should be considered.

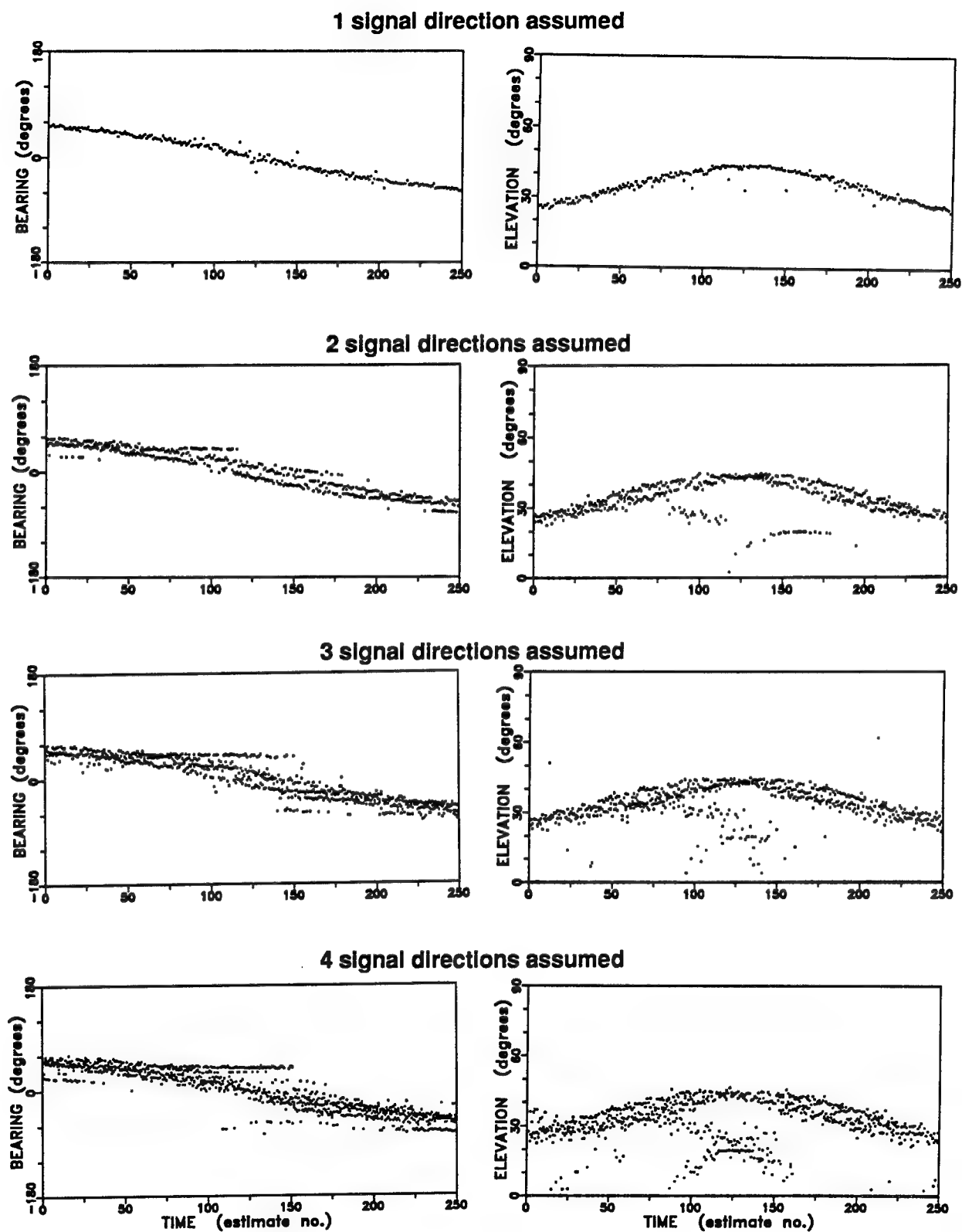


Figure 20. Time histories of estimated bearing and elevation, for the single-patch geometry of Figure 7, and a critical frequency of 7.0 MHz, as determined by the MUSIC algorithm, for various numbers of assumed signal directions.

5.2 Two Scattering Patches

5.2.1 Test Parameters

The geometry used for the MUSIC simulations is the same as that used with the plane-wave fitting, shown in Figure 13. The transmitter location and receiving array parameters are the same as for the single-patch simulations, i.e., similar to those of the Kestrel measurements. The frequency of operation is 8.0 MHz.

Apart from the two-patch geometry, all other parameters are the same as those used for the single-patch case (Section 5.1.1). The critical frequency is 7.0 MHz, which is slightly higher than the minimum needed to support propagation over the great-circle transmit-receive path.

5.2.2 Test Results

The simulations were run with for the assumed number of signal directions set to 2, 3, 4, and 5. Figure 21 gives the time histories of the bearing and elevation estimates obtained. These results may be compared with those found using plane-wave fitting with the same geometry and (7.0 MHz) critical frequency, in Section 4.2.4.1, Figure 14.

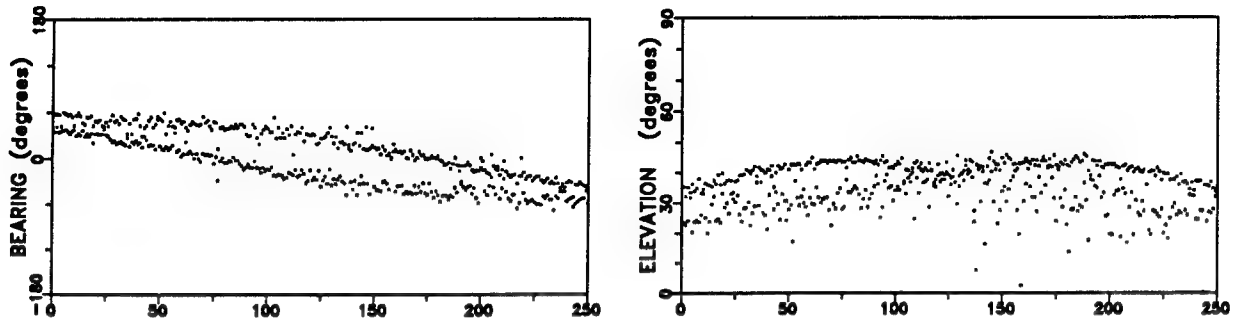
The main difference between the present results and those of plane-wave fitting, is that both patches are seen at all times during the run using the MUSIC algorithm with more than one assumed direction. The plane-wave-fitting technique tends to favour the nearer patch, giving the farther patch limited visibility especially at the start and end of the run.

When two signal directions are assumed by the MUSIC algorithm, Figure 21 shows the resultant signal directions to be slightly scattered, about two traces centered on the directions to the centers of the two patches. The spreading, as in the single-patch case for one assumed direction, is less than that observed with the plane-wave fitting.

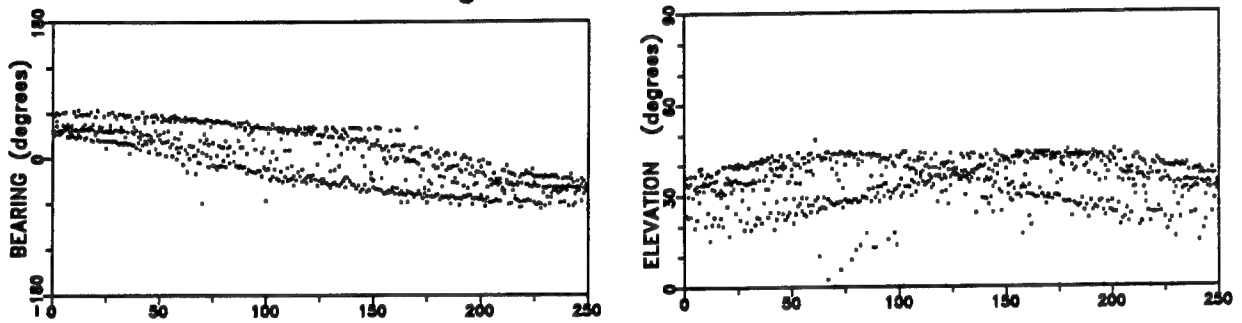
When the number of assumed signal directions increases above the number of patches, the estimated directions become more spread, so that they cover the angles subtended by the two patches. For four assumed directions, the estimates obtained tend to follow the edges of the two patches as seen at the receiving array, although this effect is not as pronounced as for a single patch and two assumed directions. For five assumed directions, the estimates tend to fill in the angles subtended by the patches, so that reasonable estimates of patch size may be obtained.

As in the single-patch case, when the number of assumed directions is increased beyond the number of patches, additional traces begin to appear which bear little relation to patch position. The bearings of these traces appear to change less with time than those associated with patch position.

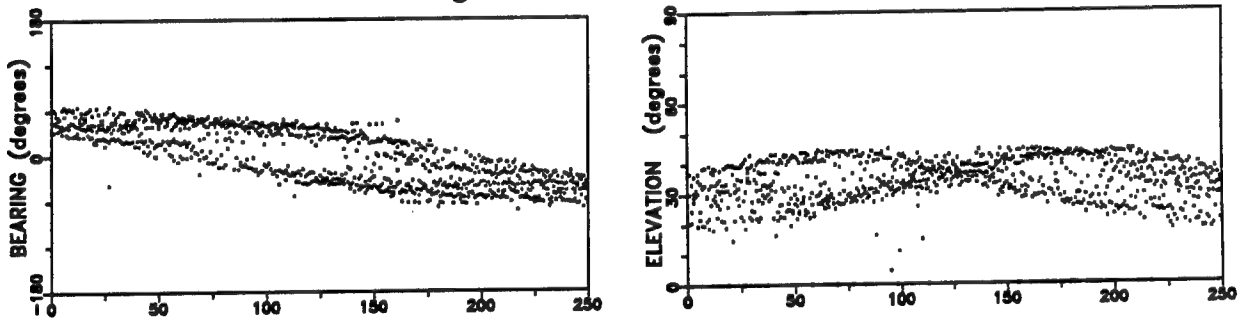
2 signal directions assumed



3 signal directions assumed



4 signal directions assumed



5 signal directions assumed

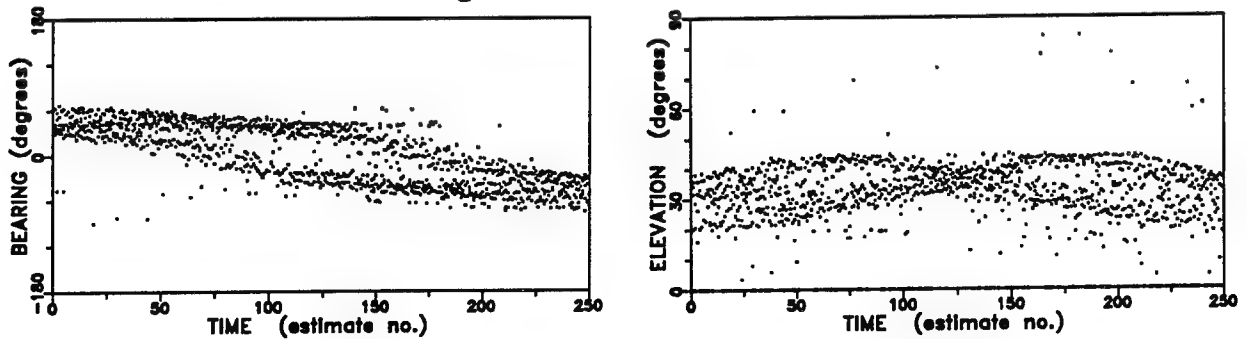


Figure 21. Time histories of estimated bearing and elevation, for the two-patch geometry of Figure 13, and a critical frequency of 7.0 MHz, as determined by the MUSIC algorithm, for various numbers of assumed signal directions.

5.3 Summary and Discussion of Findings

The simulations show that the MUSIC algorithm, when applied to scatter propagation from an extended source, has certain advantages over the plane-wave fitting algorithm. When several patches are present at the same time, it is easier to detect the presence of each with the MUSIC algorithm which can look for several signal directions at once. Further, a clearer picture of the presence and extent of an extended scattering region is obtained with MUSIC in a relatively short sampling time.

However, the MUSIC algorithm appears to be prone to providing false direction estimates, exemplified by the additional traces of Figures 20 and 21. These additional traces are most likely a result of the mismatch between the small number of signal directions assumed by MUSIC and the very large number of actual signal directions from the extended scattering patches. As will be shown in the next section, they are more likely to appear when the receiving array sidelobes are large. This implies that they are due to a sidelobe direction sometimes being identified as a true signal direction, which is more likely to occur when the sidelobe gain is close to that of the main lobe.

6.0 TESTS OF THE MUSIC ALGORITHM APPLIED TO FIELD-ALIGNED SCATTERING AND SPORADIC-E

In the Kestrel tests conducted in the polar cap region [9], sporadic E was identified as the means of propagation over the Thule-Alert path slightly more than 1 percent of the time. This propagation mode was characterized by very small bearing departures from great-circle, in contrast to the other propagation modes which were largely associated with scattering. Therefore it is highly desirable that this mode be identified when present, and used to obtain emitter bearings.

As mentioned in Section 4.2.4.1, a separate analysis of the performance of plane-wave fitting in the presence of two signals indicates that the plane-wave fitting technique always yields a direction close to that of the stronger signal, provided the stronger signal is 1 or more dB above the weaker signal. Thus, when several propagation modes were present, the Kestrel equipment which used plane-wave fitting always selected the stronger signal. Sudden jumps in the signal direction were a frequent occurrence in the Kestrel data; these were likely due to changes in the relative strength of different propagation modes. The nature of many of these signals suggests that they were likely due to scattering from extended patches.

The plane-wave fitting restricted visibility of sporadic-E to those times when it was the strongest mode. It is worth examining other techniques such as MUSIC that may increase the visibility of this useful mode and therefore the percentage of time that it may be used. The simulations presented in this section examine sporadic-E propagation along with field-aligned scattering propagation of greater strength, as seen by a receiving array employing the MUSIC algorithm.

6.1 Test Parameters

The path geometry was similar to that used for the scatter simulations of the previous section, which was based on the Kestrel measurements. The initial receiving array geometry was likewise similar to that of the Kestrel array, i.e., 7 antennas, selected from 24 antennas uniformly placed around a circle of 25 m radius; However, later simulations used other geometries. The operating frequency was 8 MHz.

The ionospheric, scatterer, and signal sampling parameters were the same as in Section 5. The sporadic-E reflection coefficient was initially set so that the received signal power from sporadic E was 7 to 10 dB below the power received from field-aligned scattering.

In general, the simulations were repeated with different numbers of assumed signal directions to be estimated.

6.2 Test Results

6.2.1 Single Scattering Patch, Sporadic E and Kestrel Array Geometry

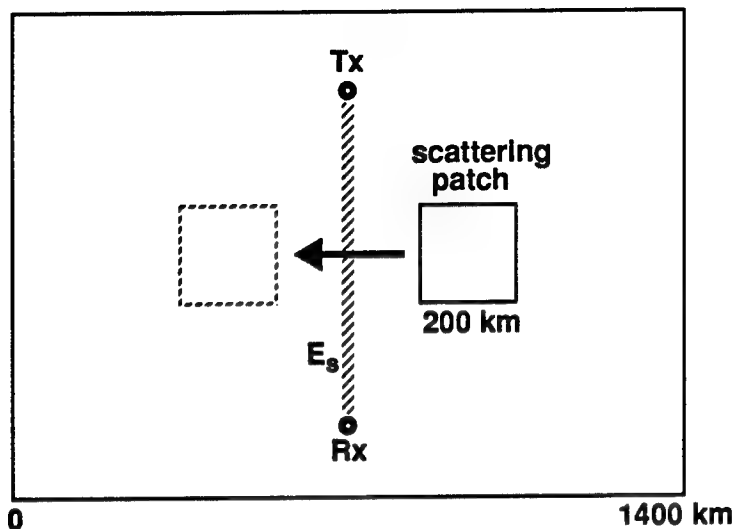


Figure 22. Plan view of geometry used for single-patch-plus-sporadic E simulations.

A plan view of the geometry used in these initial simulations is shown in Figure 22. The ionospheric critical frequency was 7.0 MHz, which allowed F-layer propagation along the great circle. A sporadic-E reflection coefficient of 0.001 was used; this value provided a sporadic-E signal power that was 7 dB below the mean signal power from the scattering patch. A series of 250 estimates were made, with a 2-km shift in patch position between estimates.

The results of the MUSIC analysis are shown in Figure 23. Time histories of the estimated bearings and elevations are shown, for two, three, and four assumed signal directions.

When only two signal directions are assumed, one of those directions follows the moving scattering patch, and the other fluctuates about the (0° bearing, 16° elevation) direction of the sporadic-E signal. There is a large amount of scatter in both traces, so that even the sporadic-E trace does not provide an accurate bearing over the short term. (A few of the low-elevation points appear to lie exactly along a 12° elevation line; these points correspond to bearings near 0° and may be an artifact of the direction-assignment procedure.)

When the number of signal directions in each estimate is increased to three, the directions begin to be better defined. Two of the traces appear to follow the edges of the patch, as previously noted in Figure 20 Section 5.1.2 for the single scattering patch only with two estimated directions. The other trace remains fixed on the sporadic-E direction, providing a good estimate of the transmitter bearing. However near the start and end of the run, when the patch is well away from the sporadic-E bearing, there is a tendency for the third direction estimate to follow the scattering patch rather than the weaker sporadic-E signal. The sporadic-E trace only becomes clearly visible when the scattering patch moves closer in direction.

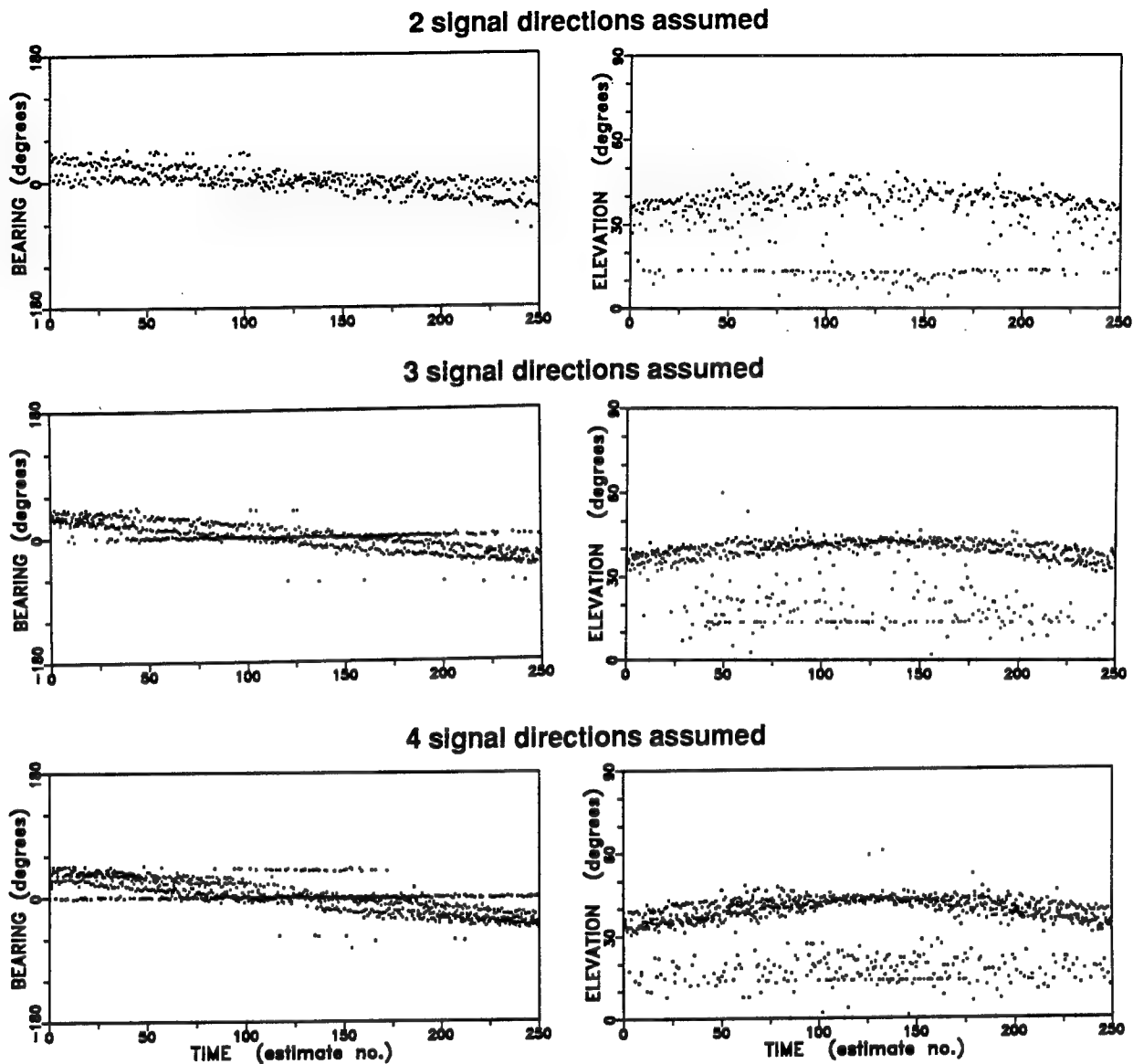


Figure 23. Time histories of estimated bearing and elevation, for the geometry of Figure 22, and a critical frequency of 7.0 MHz, as determined by the MUSIC algorithm, for various numbers of assumed signal directions.

When four signal directions are assumed, the sporadic-E trace is visible throughout the run and very constant in azimuth. The scattering patch uses the remaining three directions estimated, so that it appears in the time histories as a range of bearing and elevations which reflect the actual extent of the patch subtended at the receiving array. Near the center of the run, an additional trace appears, which is likely an array sidelobe effect resulting from signals arriving near 0° bearing falling in a sidelobe of the array steered to 45° bearing, and being incorrectly attributed to that direction. (The calculated radiation patterns for the Kestrel array geometry at 8 MHz show that when the array is steered to 45° bearing and a low elevation angle, a large sidelobe exists near 0° bearing and 45° elevation, which is the scattering patch direction near the center of the run).

6.2.2 Two Scattering Patches, Sporadic E and Kestrel Array Geometry

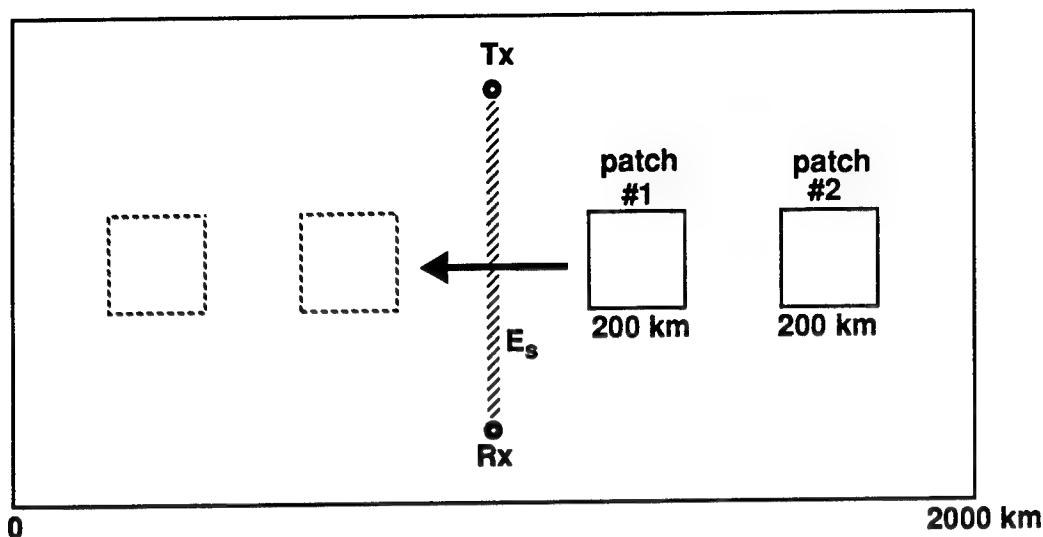


Figure 24. Plan view of geometry used for two-patch-plus-sporadic E simulations.

Figure 24 shows the geometry used for many of the two-patch simulations. In this geometry, the patches follow one another across the midpoint of the great-circle transmit-receive path, at right angles to the great circle. The sporadic E reflection coefficient of 0.001 resulted in the sporadic-E signal being approximately 10 dB below the signal received from the two scattering patches. A simulation run consisted of 250 estimates, with a 4-km shift in the patch location between estimates.

The resulting time histories of estimated bearing and elevation are shown in Figure 25 for two, three, four, and five assumed signal directions.

When two signal directions are assumed by the MUSIC algorithm, the estimates tend to follow the positions of the two scattering patches. For the main part of the run, the sporadic-E propagation is masked by the stronger signals from the scattering patches, with one assumed direction allocated to each of the scattering patches. Near the beginning and end of the run, however, the signal from the furthest scattering patch is weaker, and the sporadic-E propagation (near 0° bearing) begins to be visible.

When three signal directions are assumed, the additional direction is allocated to the sporadic-E propagation so that it becomes visible throughout the run. However the directions observed are somewhat scattered about the true direction of 0° bearing. When the assumed directions are increased to four, the sporadic-E propagation becomes more clearly defined, but some scattering in direction remains; two of the assumed directions tend to be appropriated by the nearer scattering patch and one by the further patch. With five assumed directions both patches are well-defined by two directions; the remaining direction is then free to provide a fairly well-defined sporadic-E trace with little scattering in bearing.

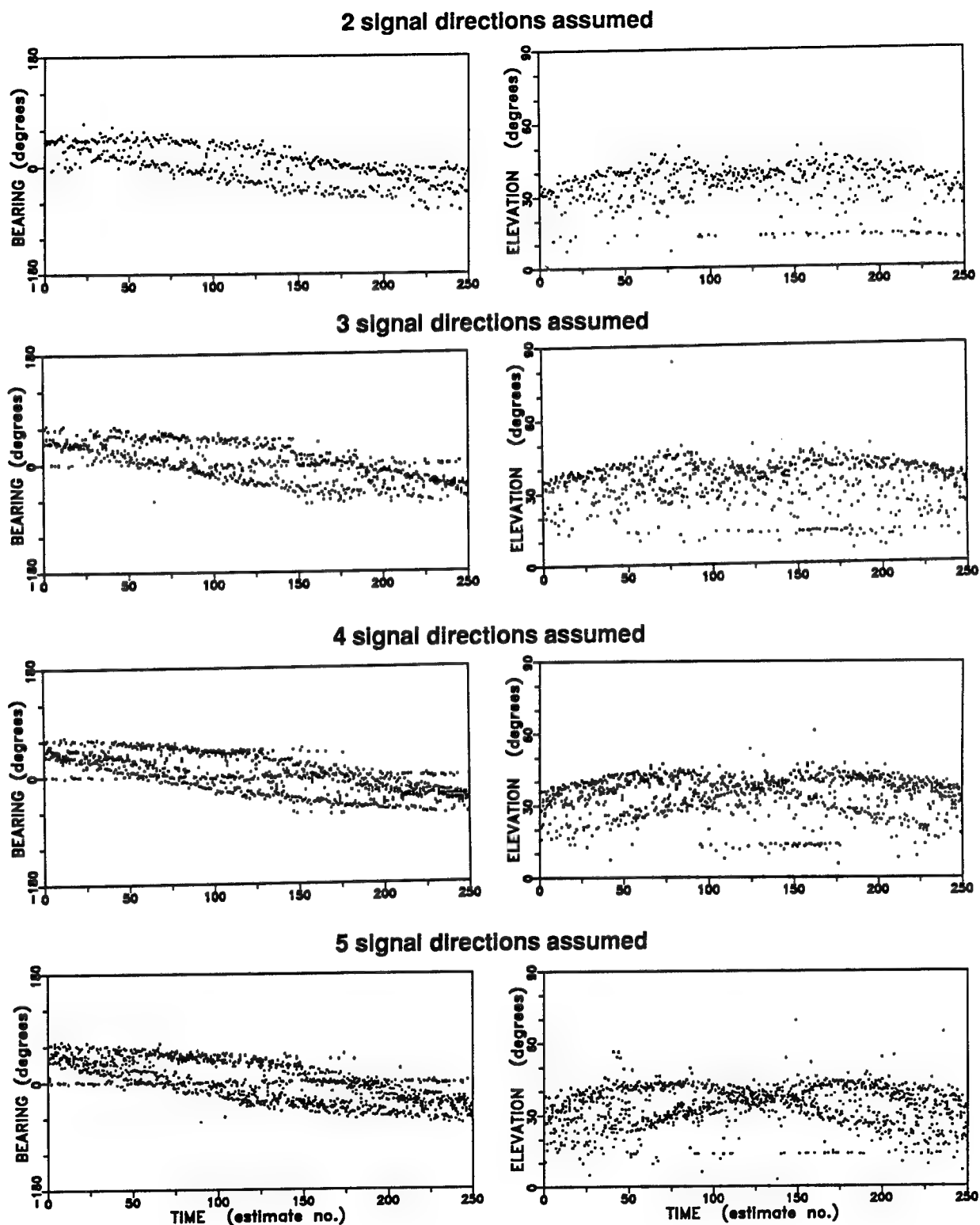


Figure 25. Time histories of estimated bearing and elevation, for the two-patch plus E_s geometry of Figure 24, and a critical frequency of 7.0 MHz, as determined by the MUSIC algorithm using the Kestrel array, for various numbers of assumed signal directions.

6.2.3 Effect of Antenna Array Geometry

In order to explore the impact of geometry on DF performance in the presence of scattering and sporadic-E propagation, other array geometries were modelled. The log-spiral geometry of the Vortex array currently being used for sampled-aperture DF tests in the Ottawa area was used.

The Vortex array consists of fifteen vertical whip elements, with the first element at a radius of 14.76m from the spiral center. The position of each succeeding element is increased in radius by 1.23 times and rotated clockwise about the center by an angle of $2\pi/7$. Normally a consecutive sequence of elements (less than fifteen) is chosen for a particular period of operation, with the sequence position within the array determined by the operating frequency, inner elements being selected for high frequencies and outer elements for low frequencies.

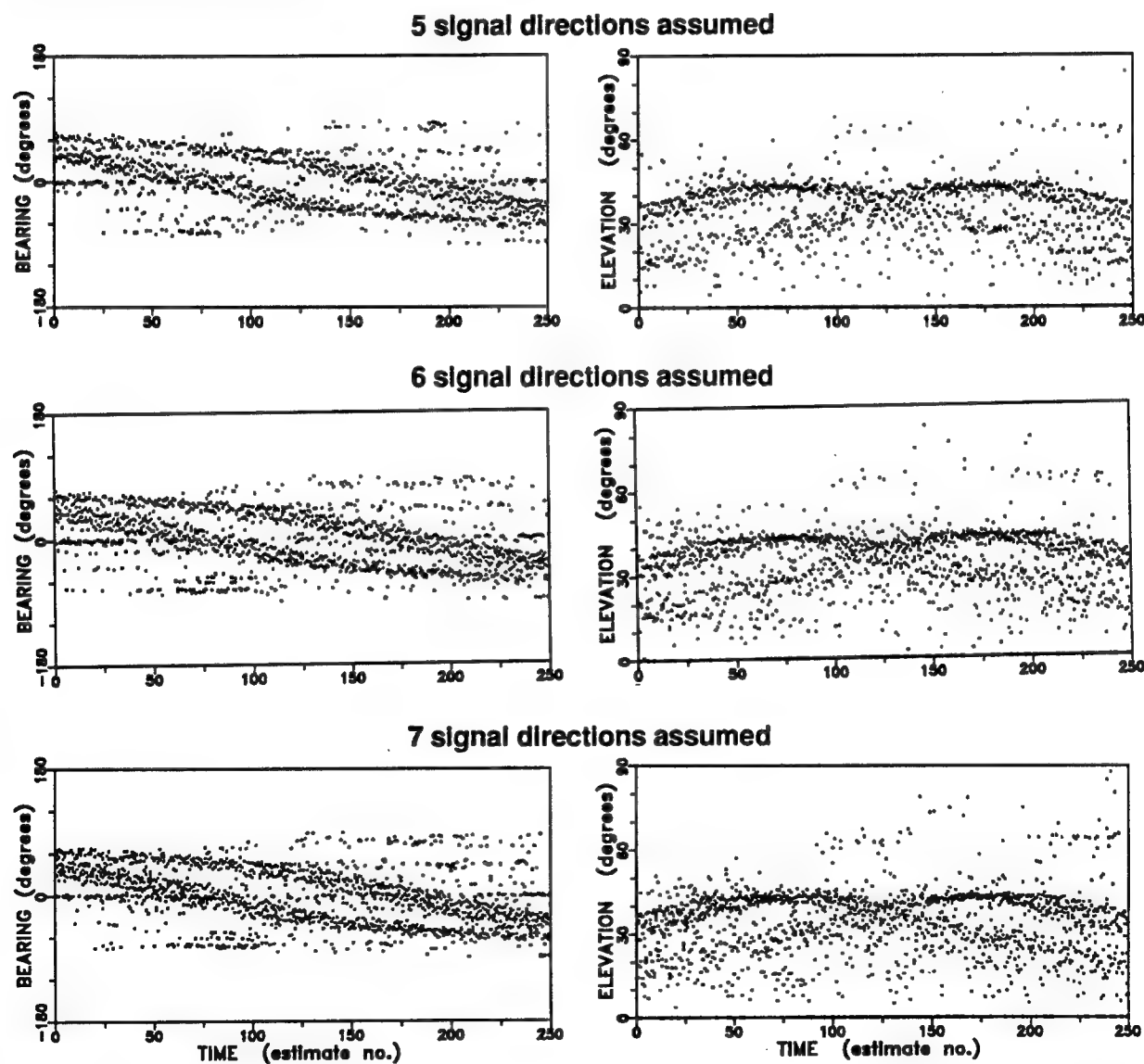


Figure 26. Time histories of estimated bearing and elevation, for the geometry of Figure 24 and a critical frequency of 7.0 MHz, as determined by the MUSIC algorithm using the 10 middle Vortex array elements, for various numbers of assumed signal directions.

As an initial selection, ten consecutive elements from the middle portion of the fifteen-element array were selected for study. This corresponded to an array for which the smallest radius was 27.47 m and the largest, 176.99 m. These dimensions and most of the resultant element spacings are considerably larger than those of the Kestrel array.

Figure 26 shows the time histories for the bearing and elevation estimated by MUSIC with 5, 6, and 7 assumed signal directions, for the 10-element Vortex array geometry. The propagation geometry and parameters used were those of the two-patch case covered in the previous section.

The capacity of this array for seeing the weaker sporadic-E propagation path in the presence of the relatively stronger scattering propagation is disappointing. The sporadic-E path near 0° bearing is visible only near the start and end of the run; in between those times when the scattering patches are crossing the great circle, it is not seen. As the number of assumed directions is increased from 5 to 7, the additional directions instead of indicating the sporadic-E propagation are appropriated by sidelobe effects similar to those discussed in Section 6.2.1.

The sidelobes of the 10-element mid-range Vortex array are relatively large at the 8.0 MHz operating frequency, certainly larger than those of the Kestrel array. Thus the response of the array when steered in a direction having a sidelobe directed toward a scattering patch is likely to be stronger than the response when steered toward the sporadic-E direction. In addition, the narrower array beamwidths present for a single steered direction imply that a scattering patch having a particular spread in direction will require more directions to be allocated to it, before any remaining direction is available to point towards a weaker sporadic-E signal. The loss of visibility of the sporadic-E mode is due to both the high sidelobes present, and the narrower beamwidths achieved by the larger-aperture 10-element Vortex array.

An alternative element selection was made from the Vortex array, to correct the problem. The innermost eight elements were selected. This resulted in a spiral radius which varied from 14.76 m for the innermost element to 62.87m for the outermost element. The element spacing covered a range from less than to somewhat greater than those of the Kestrel array. The sidelobes at the 8 MHz operating frequency could be expected to be considerably lower than the previous element selection.

Figure 27 shows the MUSIC-estimated bearing and elevation time histories obtained with the 8-element Vortex array geometry, for 5 assumed signal directions. As can be seen, the sporadic-E direction is very well defined and visible throughout the run. The bearing estimates are tightly clustered about the true bearing. A comparison with Figures 26 and 25 indicates this array configuration to be the best for the conditions simulated.

The results of this section show that sporadic-E visibility in the presence of stronger scattered signals is highly dependent on the array geometry. Large unfilled arrays with high sidelobes perform poorly in this regard. Smaller non-uniform arrays perform very well.

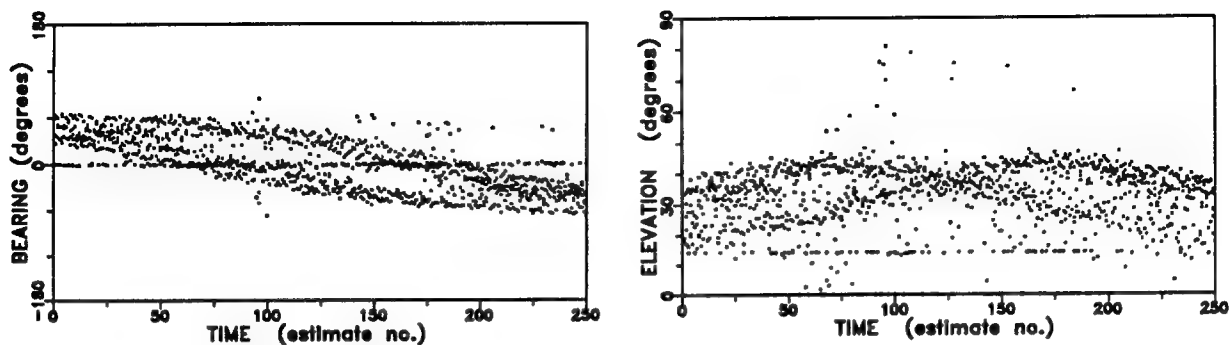


Figure 27. Time histories of estimated bearing and elevation, for the two-patch geometry of Figure 24 and a critical frequency of 7.0 MHz, as determined by the MUSIC algorithm using the 8-inner Vortex array elements, for 5 assumed signal directions.

6.2.4 Dependence on Relative Signal Strength

One factor that will influence how often sporadic-E propagation can be identified in the presence of larger scattered signals, is how much reduced in strength the sporadic-E signal can be below the scattered signals, and still be seen by the MUSIC algorithm. In order to determine this, simulations were performed for the single-scattering-patch geometry of Figure 22, using the 8-element inner Vortex array which was previously identified as being the best of the tested array configurations. The ionospheric and other parameters were the same as those used previously in this chapter, with the exception of the sporadic-E reflection coefficient which was set to various levels in order to adjust the sporadic-E signal power at the receiving array relative to the scattered signal power.

Figure 28 shows the results obtained, in terms of the bearing time histories for relative power levels $P(E_s/\text{scatter})$ of -11, -15, -21, and -26 dB.

In Figure 28, when its power is -11 dB relative to the scattered signals, the sporadic-E trace is extremely well defined, and correct in its estimated bearing. When its power is reduced further, to -15, -21, and finally -26 dB relative to scatter, the sporadic-E becomes less well-defined and precise in its estimated bearing. At -26 dB, it is questionable whether the sporadic E return could be identified as such, especially on shorter records where the scattered signals may not show much motion. However, at -21 dB, it remains sufficiently clear in its clustering to be identified.

Similar tests using the two-patch geometry of Figure 24 show that the sporadic-E propagation yields a well-defined estimated bearing trace down to signal levels of -17 dB.

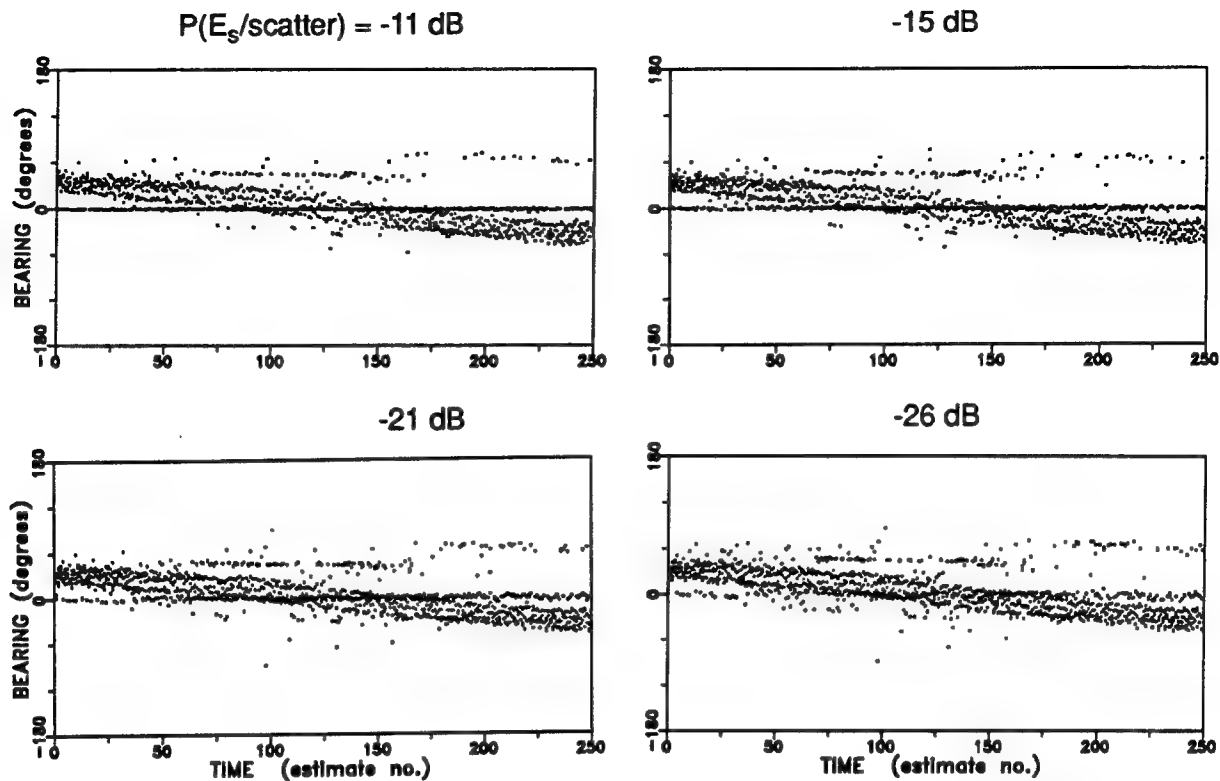


Figure 28. Estimated bearing time histories obtained with the MUSIC algorithm assuming 5 signal directions, for the single-patch geometry of Figure 22 and various sporadic-E signal powers relative to the scattered signal.

6.3 Summary and Discussion of Findings

The results clearly show that relatively weak sporadic-E propagation can be seen in the presence of stronger scattering propagation, by a sampled-aperture array employing the MUSIC algorithm. As the scattering regions provide a multiplicity of signal paths far greater than the number of paths that can be assumed by MUSIC with a small number of array elements, the scattering is only approximated by the directions found. For the scattering region sizes (200 km) and the array apertures considered (50 m at 8 MHz), it was found that with a single scattering region, it takes at least two assumed directions to approximate the scattered signals sufficiently well that a third direction could provide a good estimate of the lower-power sporadic-E signal. Thus with a single scattering patch, MUSIC must assume at least three signal directions, and with two scattering patches, five directions, in order to see the sporadic-E return well enough to identify it. (Sporadic-E can be identified by the tightly clustered constant-bearing estimates and generally low estimated elevations characteristic of E-layer propagation.)

When too many directions are assumed, the additional directions tend to be appropriated the sidelobes of the array response to the stronger signals. This is especially true if the sidelobes are close in amplitude to the main lobe. The resulting false traces in the time histories create considerable ambiguity, making sporadic-E identification difficult. Also, when the sidelobes are

large and beamwidths narrow, as for the larger-aperture unfilled 10-element Vortex array tested, the estimated directions go into the strong-scatter-signal sidelobes before going into the sporadic-E direction. The sporadic-E remains undetected.

These results present implications for the design and operation of DF arrays. While large-aperture unfilled DF arrays are appropriate for separating closely-spaced signals which come from separated transmitters on one or several propagation paths, their narrow beamwidths and large sidelobes make them inappropriate for use in high-latitude regions where extended scattering regions are a major propagation mechanism. Smaller-aperture arrays for which signals scattered from an extended region can be approximated by plane waves from only several directions work well in these cases, permitting weaker signals such as sporadic-E to be observed with little ambiguity. In operating such arrays, the performance depends on the number of assumed signal directions used by the DF algorithm. The number of directions required to account for the scattering will depend on the number and extent of the scattering regions. It is important for the operational procedure to include estimates for different numbers of assumed directions, so that the optimum for any particular time can be attained.

ACKNOWLEDGEMENTS

The assistance of M. B. Jorgenson and K. W. Moreland, regarding the sample to sample changes in the scattering propagation is gratefully appreciated. Thanks are also due to H. G. James and L. E. Montbriand for their helpful suggestions in preparing this report.

REFERENCES

- [1] Friis-Christensen, E., Y. Kamide, A.D. Richmond, and S. Matsushita (1985)
Interplanetary Magnetic Field Control of High-Latitude Electric Field Models.
J. Geophys. Res., **90**, A2 (1985), 1325-1338.
- [2] Heppner, J.P., and N.C. Maynard (1987)
Empirical High-Latitude Electric Field Models.
J. Geophys. Res., **92**, A5 (1987), 4467-4489.
- [3] Tsunoda, Roland T. (1988)
High-Latitude F Region Irregularities: A Review and Synthesis.
Rev. Geophys., **26**, 4 (1988), 719-760.
- [4] Muldrew, D.B., and J.F. Vickrey (1982)
High Latitude F Region Irregularities Observed Simultaneously with ISIS 1 and the Chatanika Radar.
J. Geophys. Res., **87**, A10 (1982), 8263-8272.
- [5] Vickrey, J.F., and M.C. Kelley (1982)
The Effects of a Conducting E Layer on Classical F Region Cross-Field Plasma Diffusion.
J. Geophys. Res., **87**, A6 (1982), 4461-4468.
- [6] James, H.G. (1989)
ISIS 1 Measurements of High-Field Backscatter Inside the Ionosphere.
J. Geophys. Res., **94**, A3 (1989), 2617-2629.
- [7] Jenkins, R.W., and K.W. Moreland (1992)
A Bumpy Ionospheric Model for High Latitude Propagation.
CRC Tech. Memo. DRL/TM091/92, Oct. 1992.
- [8] Jenkins, R.W. (1992)
A Field-Aligned Scattering Model for High-Latitude Propagation.
CRC Tech. Memo. DRL/TM095/92, Dec. 1992.

- [9] Jenkins, R.W. (1992)
Preliminary Analysis of Kestrel Data.
CRC Tech. Memo. DRL/TM083/92, Feb. 1992.
- [10] AWA Defence Industries Pty. Ltd. Australia (1993)
Kestrel Data Analysis: Third Progress and Final Report,
Prepared under contract 36001-1-3607/01-SV for the government of Canada,
Mar. 1993.
- [11] Haykin, Simon (1991)
Adaptive Filter Theory, Englewood Cliffs, N.J., Prentice Hall, 1991, 452-458.
- [12] Davies, Kenneth, (1990)
Ionospheric Radio, London, Peter Peregrinus Ltd., 1990, chapter 3.
- [13] McNamara, Leo F. (1991)
The Ionosphere: Communications, Surveillance, and Direction Finding,
Malabar, Fl., Kreiger Publishing, 1991, 39-40.
- [14] Booker, H.G., and D.C. Miller (1980)
Weak Scattering Theory Applied to Equatorial Ionospheric Scintillation for a Wide
Range of Parametric Values.
J. Atmos. Terr. Phys., **42** (1980), 189-203.
- [15] Jorgenson, M.B. (1993)
personal communication.

DOCUMENT CONTROL DATA

(Security classification of title, body of abstract and indexing annotation must be entered when the overall document is classified)

1. ORIGINATOR (the name and address of the organization preparing the document. Organizations for whom the document was prepared, e.g. Establishment sponsoring a contractor's report, or tasking agency, are entered in section 8.) COMMUNICATIONS RESEARCH CENTRE 3701 Carling Avenue, P.O. Box 11490, Stn. H Ottawa, Ontario K2H 8S2		2. SECURITY CLASSIFICATION (overall security classification of the document including special warning terms if applicable) UNCLASSIFIED	
3. TITLE (the complete document title as indicated on the title page. Its classification should be indicated by the appropriate abbreviation (S,C or U) in parentheses after the title.) A SIMULATION STUDY OF HF DIRECTION FINDING IN THE PRESENCE OF F-REGION SCATTERING AND SPORADIC - E (U)			
4. AUTHORS (Last name, first name, middle initial) JENKINS, ROBERT W.			
5. DATE OF PUBLICATION (month and year of publication of document) JANUARY 1994	6a. NO. OF PAGES (total containing information. Include Annexes, Appendices, etc.) 60	6b. NO. OF REFS (total cited in document) 15	
7. DESCRIPTIVE NOTES (the category of the document, e.g. technical report, technical note or memorandum. If appropriate, enter the type of report, e.g. interim, progress, summary, annual or final. Give the inclusive dates when a specific reporting period is covered.) CRC REPORT			
8. SPONSORING ACTIVITY (the name of the department project office or laboratory sponsoring the research and development. Include the address.) DEFENCE RESEARCH ESTABLISHMENT OTTAWA OTTAWA, ONTARIO, K1A 0Z4			
9a. PROJECT OR GRANT NO. (if appropriate, the applicable research and development project or grant number under which the document was written. Please specify whether project or grant) 1410-041BB		9b. CONTRACT NO. (if appropriate, the applicable number under which the document was written)	
10a. ORIGINATOR'S DOCUMENT NUMBER (the official document number by which the document is identified by the originating activity. This number must be unique to this document.) CRC REPORT 93-004		10b. OTHER DOCUMENT NOS. (Any other numbers which may be assigned this document either by the originator or by the sponsor) CRC Report #93-004	
11. DOCUMENT AVAILABILITY (any limitations on further dissemination of the document, other than those imposed by security classification) <input checked="" type="checkbox"/> (X) Unlimited distribution <input type="checkbox"/> () Distribution limited to defence departments and defence contractors; further distribution only as approved <input type="checkbox"/> () Distribution limited to defence departments and Canadian defence contractors; further distribution only as approved <input type="checkbox"/> () Distribution limited to government departments and agencies; further distribution only as approved <input type="checkbox"/> () Distribution limited to defence departments; further distribution only as approved <input type="checkbox"/> () Other (please specify):			
12. DOCUMENT ANNOUNCEMENT (any limitation to the bibliographic announcement of this document. This will normally correspond to the Document Availability (11). However, where further distribution (beyond the audience specified in 11) is possible, a wider announcement audience may be selected.)			

UNCLASSIFIED

SECURITY CLASSIFICATION OF FORM

13. **ABSTRACT** (a brief and factual summary of the document. It may also appear elsewhere in the body of the document itself. It is highly desirable that the abstract of classified documents be unclassified. Each paragraph of the abstract shall begin with an indication of the security classification of the information in the paragraph (unless the document itself is unclassified) represented as (S), (C), or (U). It is not necessary to include here abstracts in both official languages unless the text is bilingual).

An HF direction finding (DF) system employing sampled-aperture techniques on high-latitude signals is simulated. The propagation is treated as scatter from moving patches of field-aligned F-region irregularities modelled as vertical "thin-wire" scatterers in a horizontally stratified ionosphere, plus a weak sporadic-E (E_s) reflection from a horizontal mirror-like surface. The resultant simulated received signals are analyzed by plane wave fitting and multiple-signal classification (MUSIC) DF algorithms.

Simulations of DF operations on scattered signals, using system parameters similar to those used for actual high-latitude observations, reveal results similar to those observed. The observed directions reflect the locations of the scattering patches rather than the transmitter. The detection of a patch depends strongly on its location, the radio frequency, and the ionospheric parameters. When a patch is seen, the time history of estimated directions indicated its width, as well as its location. MUSIC provides a picture of the width and number of scattering patches present in a short time. Plane-wave fitting tends to give only the directions for the patch having the strongest scattered signal and requires a longer time for the successive direction estimates (spread over the angle subtended by the patch) to indicate the patch width. When too many signal directions are assumed, MUSIC gives false directions which correspond to the steered directions of the array for which the larger sidelobes are pointed toward the strongest signals. When a weaker E_s signal is present with the scattered signal, MUSIC can see it clearly and provide a good direction estimate, provided array dimensions are not so large that narrow beamwidths coupled with large-sidelobe effects prevent the weaker E_s signal from being seen.

14. **KEYWORDS, DESCRIPTORS or IDENTIFIERS** (technically meaningful terms or short phrases that characterize a document and could be helpful in cataloguing the document. They should be selected so that no security classification is required. Identifiers, such as equipment model designation, trade name, military project code name, geographic location may also be included. If possible keywords should be selected from a published thesaurus. e.g. Thesaurus of Engineering and Scientific Terms (TEST) and that thesaurus-identified. If it is not possible to select indexing terms which are Unclassified, the classification of each should be indicated as with the title.)

HF Direction Finding
Direction Finding
HF propagation
High-Latitude Ionosphere

UNCLASSIFIED

SECURITY CLASSIFICATION OF FORM